EYE-CLIMA
Verifying emissions of climate forcers

Black carbon emissions and uncertainties globally: final estimates

DELIVERABLE 3.11

Author(s):	Sabine Eckhardt, Angelos Gkouvousis, Maria Kanakidou
Date of submission:	30-06-2026
Version:	1.0
Responsible partner:	University of Crete, NILU
Deliverable due date:	31-12-2025
Dissemination level:	Public

Call:	HORIZON-CL5-2022-D1-02
Topic:	Climate Sciences and Responses
Project Type:	Research and Innovation Action
Lead Beneficiary:	NILU - Norsk Institutt for Luftforskning

This project has received funding from the European Union's Horizon Europe research and innovation programme under grant agreement No 101081395

Document History

Version	Date	Comment	Modifications made by
0.1	26-05-2026	First Draft	Angelos Gkouvousis (UoC) Maria Kanakidou (UoC) Sabine Eckhardt (NILU)
0.2	04-06-2026	Sent for Internal review	Maria Kanakidou (UoC)
0.3	05-06-2026	Internal review	Rona Thompson (NILU)
1.0	26-06-2026	Final revised version	Angelos Gkouvousis (UoC) Maria Kanakidou (UoC) Sabine Eckhardt (NILU)

This project has received funding from the European Union's Horizon Europe research and innovation programme under grant agreement No 101081395

Summary

Black carbon (BC) is a short-lived climate forcer and the main absorbing component of atmospheric aerosols, the others being brown carbon and dust. BC contributes to global warming and is also an atmospheric pollutant harmful to human health. BC is produced during incomplete combustion of organic matter. Improving knowledge of BC emissions is needed for implementation of policy to mitigate climate change and for clean air.
This deliverable presents the results of atmospheric inversions to improve estimates of BC emissions globally. Two atmospheric transport models are used for BC in EYECLIMA, a Lagrangian particle dispersion model, FLEXPART, and an Eulerian global chemistry transport model, TM5MP, which are used with the Bayesian inversion frameworks, FLEXINVERT and TM5MP-CTDAS, respectively. Ground-based observations of elemental carbon (EC) and equivalent black carbon (eBC) have been collected and used to optimize the emissions via atmospheric inversions. Accessible observations are, however, relatively scarce over South America, Africa and Asia.

This deliverable provides the final BC emission estimates based on multi-year inversions for the studied period from 2015-2023. As such, this deliverable represents an update to the previously submitted deliverable, D3.7, which presented preliminary results from global inversions performed for 2017. Since D3.7, additional observations have been collected and are used in the inversions presented in this deliverable.

Both modelling frameworks calculated lower global posterior than prior emissions after 2020, while from 2015 to 2019 the global posterior emissions calculated by FLEXINVERT are higher than the prior emissions. TM5MP-CTDAS calculates consistently lower posterior than prior BC emission across all studied years. The range of the posterior emission estimates calculated by the TM5MP-CTDAS 50 ensemble members is rather large and comprises the posterior emission estimates by FLEXINVERT.

However, there is still a lack of available observations in Asia, Africa and South America and improving data coverage in these regions would increase the confidence in the inversion results there.

This project has received funding from the European Union's Horizon Europe research and innovation programme under grant agreement No 101081395

TABLE OF CONTENTS

This project has received funding from the European Union's Horizon Europe research and innovation programme under grant agreement No 101081395

1. Introduction

Black Carbon (BC) refers to atmospheric particles containing a carbon-based sooty core and are produced by incomplete combustion. BC is the major absorbing component of atmospheric aerosols and contributes an estimated ~0.1°C to global warming (IPCC AR6). BC, being fine particles, can also pass into the human respiratory system and negatively impact human health. As such, BC emissions are relevant for both human health and the climate and reducing its emissions would have a dual benefit.

BC not only influences radiative forcing but also modulates cloud formation, the climate impact of which is difficult to assess, thus the uncertainty in BC's contribution to global warming is evaluated to be very high (IPCC 6th Assessment Report, AR6). In addition, BC is an aerosol with large uncertainties in its emission due to the uncertainty in the emission factors on which emission inventories are built. To constrain the emissions, accurate and abundant observations are needed. Unfortunately, it is not possible to make measurements of BC directly. Usually, equivalent BC (eBC) is determined by using the aerosol absorption coefficient (AAC). Another approach is to use thermo-optical or laser-based methods, which measure carbon's resistance to heat and the measured quantity is referred to as elemental carbon (EC). Inter-comparisons have shown that these methods do not give the same results and can vary by a factor of 3, indicating a need to better describe BC.

Globally, BC emissions are estimated at 6 million tons per year with a large uncertainty (Figure 1). Most anthropogenic emissions are found in India, whereas most natural emissions are found in Equatorial Africa.

Furthermore, in Northern China high-resolution wintertime observations from Shijiazhuang between 2018 and 2020 showed a marked decrease in BC concentrations from over 9 μg/m³ to 3.5 μg/m³, reflecting the success of air quality policies (Wang et al., 2023). Source attribution indicated a shift from biomass burning dominance in 2018 to fossil fuel combustion in the subsequent years. With the help from trajectory analyses, it was confirmed that both local emissions and regional transport from nearby industrial areas, like central Shanxi, contributed to the observed BC levels. The study also noted the importance of considering both climate and air quality synergies in mitigation strategies, as some BC reduction measures may conflict with CO_2 emission goals.

For India, measurements from fifteen sites in the India Meteorological Department's BC observation network during 2016–2018 demonstrated high variability across the subcontinent (Kumar et al., 2020). Northern India and the Indo-Gangetic Plain recorded the highest BC mass concentrations, with annual means exceeding 13,000 ng/m³ in Delhi. In contrast, coastal and background stations in southern India observed much lower concentrations. A source apportionment analysis using the Aethalometer model revealed that fossil fuel combustion dominated BC contributions year-round, though biomass burning played a notable seasonal role, especially in winter. Seasonal analyses showed the highest concentrations post-monsoon and in winter, which are attributed to increased domestic fuel use and stagnant meteorology, while monsoon rains reduced concentrations through wet scavenging. These results highlight the spatial heterogeneity of BC in India and the importance of addressing both fossil and biomass sources.

In order to study BC concentrations and trends on a global or regional basis, often a combination of satellite observations and surface stations is used. In this manner, significant spatial and temporal variability influenced by regional emission sources, policy interventions, and measurement approach, can be revealed. For example, for China (Zhao et al., 2024) a comprehensive analysis combining satellite data from the Ozone Monitoring Instrument (OMI), a top-down inversion method, and an exposure–response model examined BC trends from 2000 to 2020. Zhao et al. (2024) found that bottom-up inventories likely underestimated BC emissions, particularly in less-developed western regions. This study found that national emissions rose by

This project has received funding from the European Union's Horizon Europe research and innovation programme under grant agreement No 101081395

8% during 2000–2010 but declined by 26% from 2010–2020 due to pollution control measures. While some industrial provinces saw emissions rebound after initial reductions, more urbanized regions experienced sustained decreases.

Also, for India satellite-based approaches further extend our understanding of BC distributions. A study using the Cloud and Aerosol Imager-2 (CAI-2) aboard GOSAT-2 validated satellite retrievals of BC over India against ground-based data from the ARFINET (Gogoi et al., 2023) network. The results showed good agreement, with RMSE values below 1 μg/m³ and high correlations during winter and pre-monsoon months. These satellite observations revealed regional BC hotspots and allowed for the extrapolation of spatiotemporal patterns globally. Areas with intense biomass burning showed elevated BC concentrations, supporting the use of satellite products for continuous monitoring of anthropogenic and fire-related emissions.

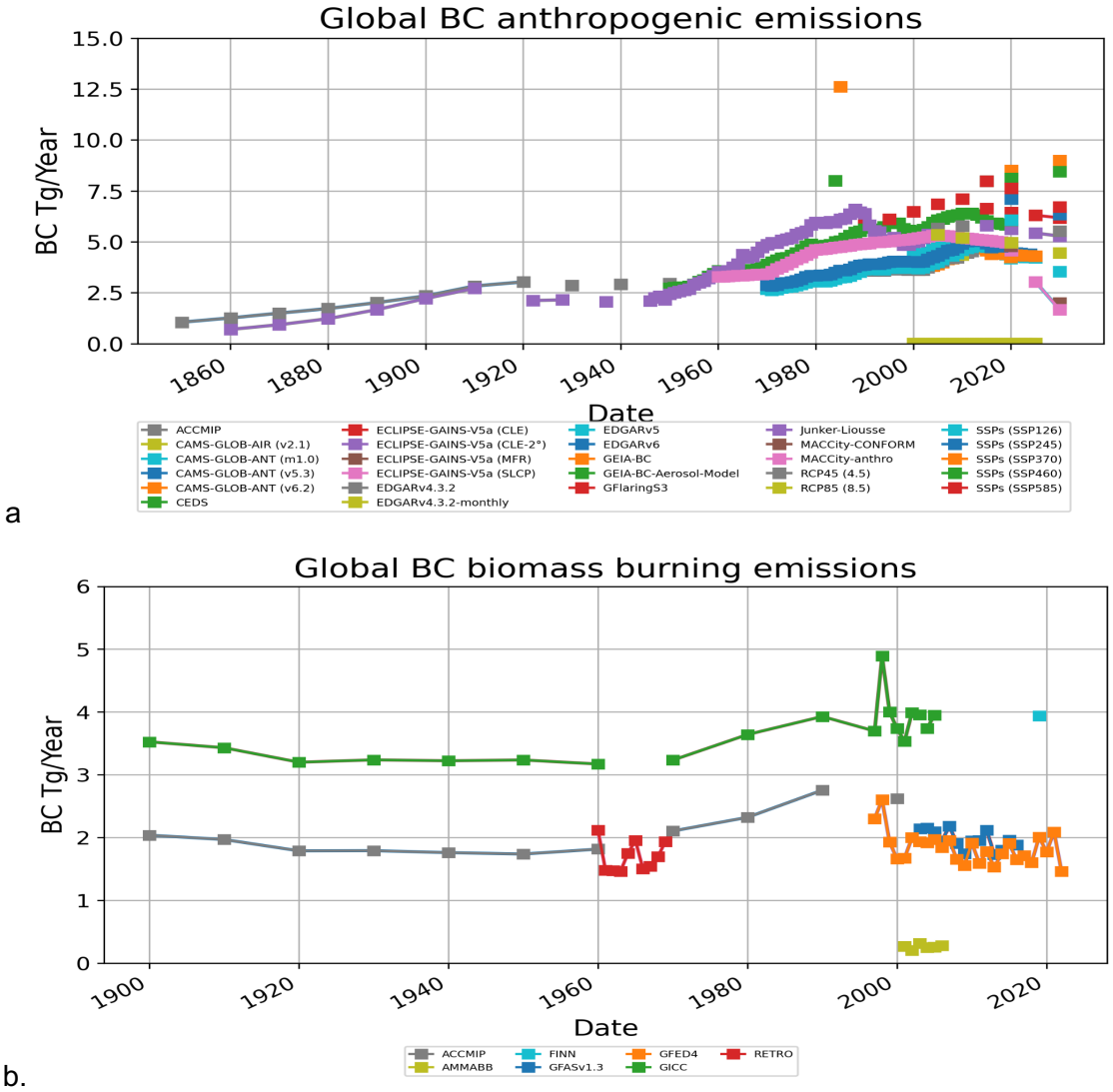

Figure 1. Current state of BC emissions in global emission inventories (source of data: eccad.aeris-data.fr) (a) anthropogenic emissions, (b) biomass burning emissions.

This project has received funding from the European Union's Horizon Europe research and innovation programme under grant agreement No 101081395

Another satellite study utilized the Earth Polychromatic Imaging Camera (EPIC) on DSCOVR to analyze smoke aerosols over North America and central Africa, focusing on BC and brown carbon (BrC) content (Choi et al., 2024). Using the MAIAC algorithm, researchers retrieved aerosol optical properties and inferred BC and BrC volume fractions with high spatial and temporal resolution. The results demonstrated that smoke over North America, primarily from wildfires, exhibited high aerosol layer heights and substantial BrC content, whereas smoke in central Africa, largely from savanna burning, showed stronger absorption and higher BC fractions. Regional differences in aerosol optical depth and single-scattering albedo were closely linked to the type of burning and local meteorological conditions. These findings provide critical observational constraints for climate modeling and reinforce the role of satellite data in assessing the radiative impacts of light-absorbing aerosols.

Recently, Yang et al (2025) developed a simultaneous inversion algorithm for four carbonaceous aerosol components: black carbon (BC), brown carbon (BrC), water-soluble organic matter and water-insoluble organic matter. They considered distinct optical, solubility, and hygroscopicity properties of each of these four aerosol components. They used the AERONET observations together with their inversion algorithm impeded in the GRASP model to invert global concentrations for 2022 and found that BC maximized in South Asia.

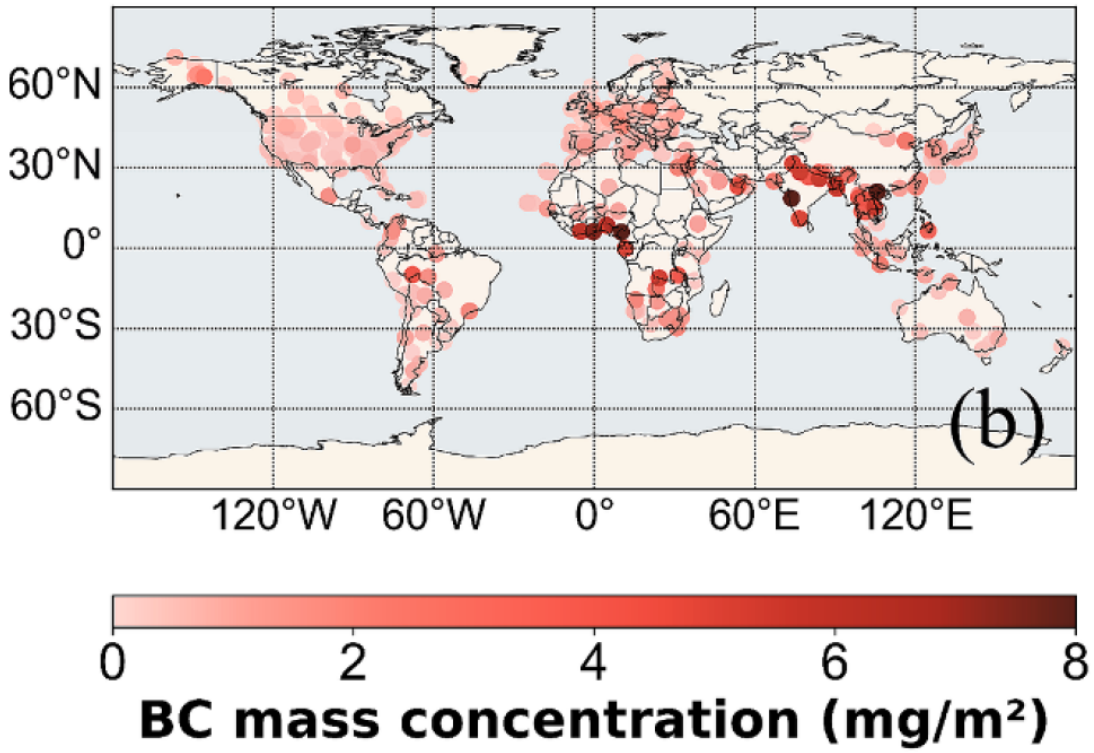

Figure 2. Annual average mass concentration of BC at AERONET stations from Yang et al. 2025; https://doi.org/10.1016/j.envint.2025.109432)

Ren et al. (2025) used the GEOS-Chem global chemistry transport model together with the Surface Particulate Matter Network (SPARTAN) observations of BC. They found that using the Community Emissions Data System (CEDS) emission inventory the observed BC variability in SPARTAN measurements was well represented by the model across the developed regions with low BC concentrations but BC was

This project has received funding from the European Union's Horizon Europe research and innovation programme under grant agreement No 101081395

underestimated by 38% across high-BC regions in the Global South. Similar discrepancies were also found using the Task Force on Hemispheric Transport of Air Pollution (HTAP) inventory and the Emissions Database for Global Atmospheric Research (EDGAR) inventory, demonstrating the existing uncertainty in BC emission estimates.

Together, these studies highlight that BC concentrations and their impacts vary widely across regions and time periods. They illustrate the importance of integrating surface observations, source apportionment techniques, and satellite remote sensing to characterize BC emissions and their effects on air quality, health, and climate.

In EYECLIMA, we aimed to constrain the global BC emissions by using two different inversion frameworks. One framework is the TM5-MP, which also simulates aerosol microphysics. A data assimilation system was developed for TM5-MP using the Ensemble Kalman filter method based on the Carbon Tracker Data Assimilation Shell. The other is the FLEXPART-FLEXINVERT framework: FLEXPART models aerosol species using parameterisation of scavenging, which has been tested both for mid latitude and Arctic stations, Inversions of BC will be made using FLEXINVERT.

Both systems use observations of eBC concentration from the ACTRIS database and the NOAA/ESRL Federated Aerosol Network. We assimilated only eBC and EC observations in an effort to have as comparable input data as possible. Note that aerosol optical depth observations from the AERONET network (https://aeronet.gsfc.nasa.gov/), while they provide better global coverage than the station and campaign data, do not provide information specific to BC but to all absorbing aerosol, i.e. include brown carbon and dust. Similarly, satellite observations provide global coverage but they account for the mixture of aerosols in the atmospheric column thus estimating BC from satellite observations includes several assumptions that will introduce further uncertainty on the inversion. Although BC emissions are estimated globally, the posterior emissions are expected to be more accurate over Europe and North America due to the density of data from the observational network there. In TM5-MP, the radiative absorption of BC is also modelled and validated against data from the global AERONET database of total column AAOD, from which BC can be also derived. Inversions are performed globally at 1°×1° (TM5-MP) and on a variable grid resolution (FLEXPART) and monthly from 2015 to 2023.

This project has received funding from the European Union's Horizon Europe research and innovation programme under grant agreement No 101081395

2. Method

2.1 FLEXPART transport modelling

To investigate atmospheric transport patterns and connect them to potential source regions to be used for the inversion, simulations were conducted using the Lagrangian particle dispersion model FLEXPART (Pisso et al., 2019; Bakels et al., 2024). FLEXPART simulates the trajectories of a large ensemble of virtual particles released into the atmosphere and accounts for key atmospheric processes including turbulence-induced dispersion, deep and shallow convection, as well as both dry and wet deposition. Each released particle was tracked within the model domain for a duration of 30 days, ensuring coverage of long-range transport events. FLEXPART has been extensively evaluated for various tracers, including black carbon (BC), particularly in Arctic regions, which adds robustness to its application in this study (Zhu et al., 2020; Stohl et al., 2013). For this application the model was run continuously with three hourly resolution or coarser adapted to the observations for the whole study period from 2015 to 2022, using observations in Africa, Eurasia and America.

2.2 FLEXINVERT inversion framework

To quantify surface emissions and evaluate source strengths, the output from FLEXPART was used within the FLEXINVERT (Thompson and Stohl, 2014) inversion framework. FLEXINVERT is a Bayesian atmospheric inversion system that utilizes the source-receptor relationships (SRRs) computed by FLEXPART to constrain spatially and temporally resolved emissions based on observational data. The system integrates the modeled SRRs to prior emissions estimates to model concentrations, that are then compared to measured concentrations and applies a Bayesian optimization to estimate the most probable fluxes, taking into account both prior emission information and the uncertainties associated with the observations and the transport model. In this study, FLEXINVERT was configured to assimilate the three-hourly observational data in conjunction with the daily-resolved footprint matrices from FLEXPART, providing an optimized estimate of source strengths across the domain. This framework allows for robust quantification of emissions and identification of potential source regions, particularly valuable in regions with sparse observational coverage or complex atmospheric transport dynamics. The grid for the inversion was dynamically adapted depending on the spatial distribution of the observations. Fig. 3 shows the grid as used for the year 2017.

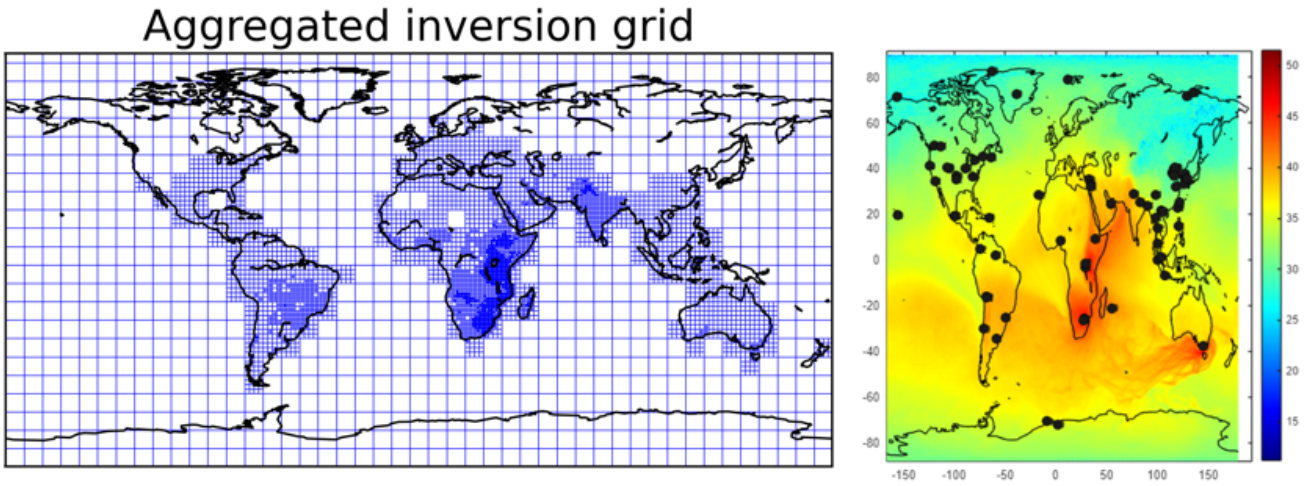

Fig. 3. Inversion grid for constraining the emission (1). Total emission sensitivity (b) for 2017 in units of log(second) derived by FLEXPART and used to determine the variable grid used in the inversion (a). The points indicate the positions of the observation sites.

This project has received funding from the European Union's Horizon Europe research and innovation programme under grant agreement No 101081395

2.3 TM5MP transport modelling

TM5MP is a Eulerian, global chemistry transport model, used to investigate the atmospheric transport of BC in the global atmosphere. It explicitly accounts for aerosol microphysics, using the M7 module. Inversions of BC will be made globally using the TM5-MP model, (Williams et al., 2017) with full chemistry and aerosol microphysics, using the M7 module (Vignati et al., 2004). The model has been extensively evaluated for various tracers and contributes to CMIP simulations. TM5MP is using ERA5 meteorology and as starting (a priori) emissions we used the CMIP6 emission inventory (Feng et al., 2020), which covers emissions from both anthropogenic activities and biomass burning events. Inversions were performed for the years 2015-2023 using the CMIP6 SSP3-7.0. The model is used as the forward model using a 1°×1° horizontal resolution and 34 vertical levels. The model uses a dynamic timestep of 30 min and 15 min for chemistry and aerosol microphysics.

2.4 TM5MP-CTDAS inversion modelling

TM5MP is coupled with the Carbon Tracker Data Assimilation Shell (CTDAS) that is using the Ensemble Kalman filter method and a fixed-lag assimilation window method (Van Der Laan-Luijkx et al., 2017) for BC inversions. In CTDAS, the forward model output using these emissions is compared with the EC and eBC observations worldwide obtained by filter-based techniques and aethalometers from the EBAS (https://ebas.nilu.no) and IMPROVE (Malm et al., 1994) databases, that were thus assimilated by CTDAS. Scaling factors for emission corrections are computed per HTAP region. An assimilation window of 1 week with a fixed-lag of 2 weeks is applied. An ensemble of 50 members, representing total BC emissions from all available sectors, is used for the assimilation for each of the 16 HTAP source regions in which emissions are optimized (Fig. 4). The model uses 50 station locations in Europe and 173 outside Europe most of them in the USA, both eBC and EC observations (Fig. 4). TM5MP uses more stations over Europe and USA than FLEXINVERT.

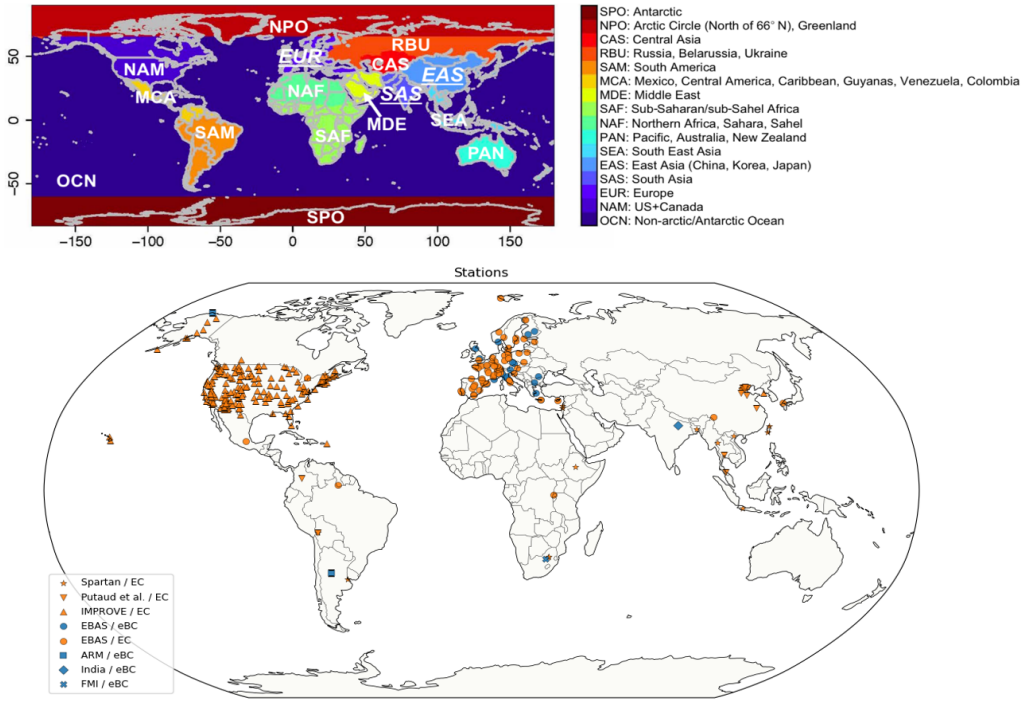

Fig. 4. Regions used in TM5MP-CTDAS for BC emission optimization (upper panel). Location of the stations with data used for the inversions of TM5MP-CTDAS reported in this deliverable (lower panel). Stations marked in blue provide equivalent BC (eBC) concentrations and stations marked in orange elemental carbon (EC) concentrations.

This project has received funding from the European Union's Horizon Europe research and innovation programme under grant agreement No 101081395

2.5 Observations

Within the EYECLIMA project, observational data on black carbon (BC) were compiled from the aethalometers retrieving AAC. To ensure consistency across different measurement protocols and instruments, the data were harmonized into a unified and quality-controlled dataset representing homogeneous BC concentrations. The resulting time series vary in length and continuity, with many stations exhibiting temporal gaps due to data availability and operational interruptions. Among the available sites, background monitoring stations were found to be the most suitable for the analysis, as they are less influenced by local pollution sources (which cannot be accurately represented with a global model) and provide a more representative signal of regional and long-range transported BC. These observations were assimilated in the inversion framework, enabling the optimization of emission estimates and evaluation of the modelled atmospheric transport and scavenging processes.

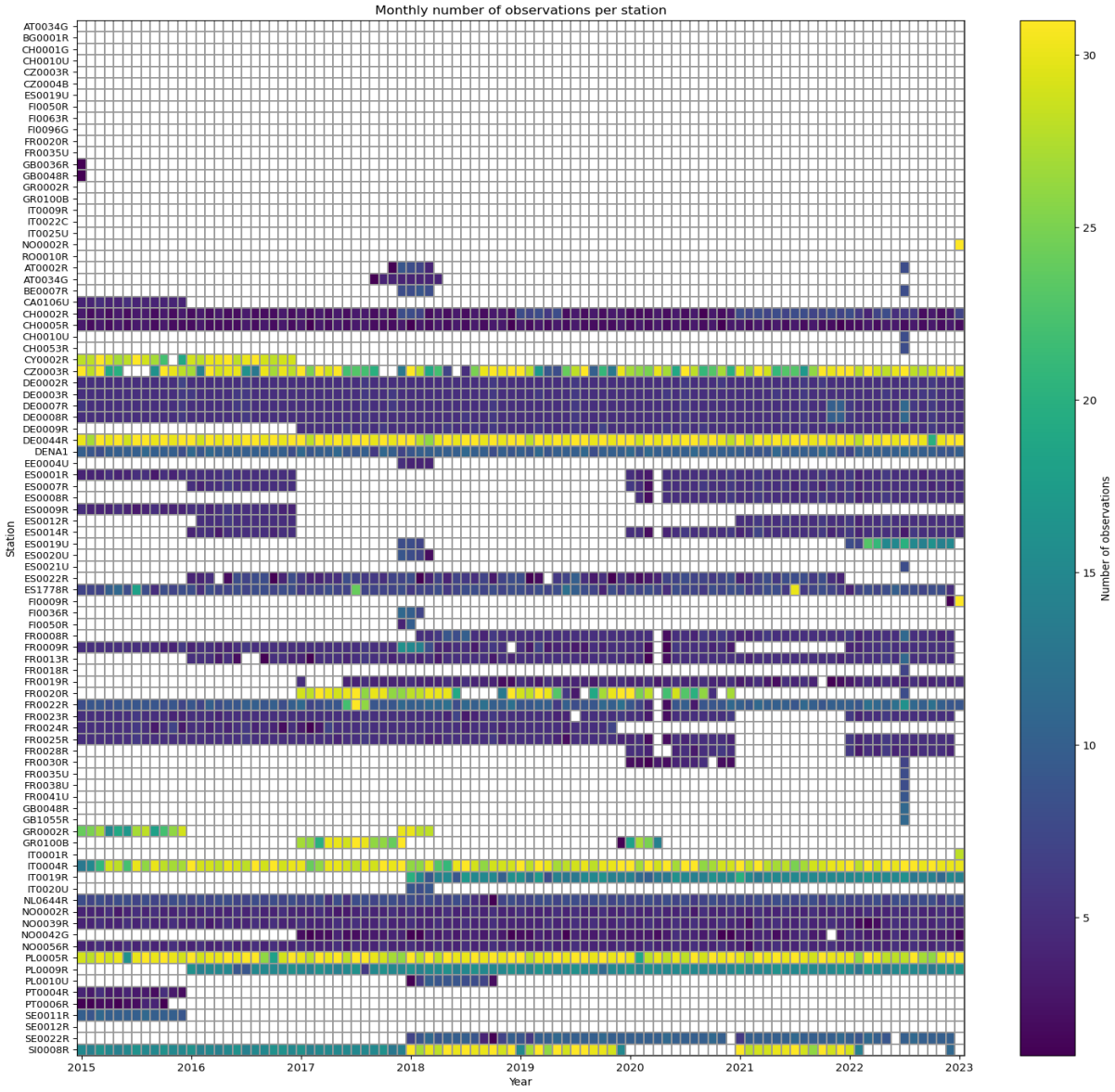

Fig. 5. EBAS stations with available BC observations for the period 2015 to 2023, the colored scale shows the number of available daily observations in each month.

This project has received funding from the European Union's Horizon Europe research and innovation programme under grant agreement No 101081395

Table 1. List of EBAS stations used.

Name	Latitude	Longitude	Altitude (m) asl	Name	Latitude	Longitude	Altitude (m) asl
AT0002R	47.77	16.77	117	FR0020R	48.71	2.15	162
AT0034G	47.05	12.96	3106	FR0022R	48.56	5.51	392
BE0007R	50.30	6.00	496	FR0023R	44.57	5.28	605
CA0106U	43.78	-79.47	198	FR0024R	47.83	-1.84	29.45
CH0002R	46.81	6.94	489	FR0025R	46.81	2.61	182
CH0005R	47.07	8.46	1031	FR0028R	48.26	-2.94	307
CH0010U	47.38	8.53	409	FR0030R	45.77	2.96	1465
CH0053R	47.19	8.18	797	FR0035U	43.31	5.39	73
CY0002R	35.04	33.06	520	FR0038U	45.16	5.74	214
CZ0003R	49.57	15.08	535	FR0041U	48.86	2.34	35
DE0002R	52.80	10.76	74	GB0036R	51.57	-1.33	137
DE0003R	47.91	7.91	1205	GB0048R	55.79	-3.24	260
DE0007R	53.14	13.03	62	GB1055R	51.15	-1.44	78
DE0008R	50.65	10.77	937	GR0002R	35.34	25.67	150
DE0009R	54.44	12.72	1	GR0100B	37.99	23.82	270
DE0044R	51.53	12.93	86	IT0001R	42.11	12.64	48
DENA1	63.72	-148.97	658	IT0004R	45.81	8.64	209
EE0004U	58.37	26.74	40	IT0009R	44.19	10.70	2165
ES0001R	39.55	-4.35	917	IT0019R	42.81	12.57	1090
ES0007R	37.24	-3.53	1230	IT0020U	45.74	7.36	560
ES0008R	43.44	-4.85	134	IT0022C	44.52	11.34	54
ES0009R	41.27	-3.14	1360	IT0025U	45.48	9.23	118
ES0012R	39.08	-1.10	885	NL0644R	51.97	4.92	1
ES0014R	41.39	0.73	470	NO0002R	58.39	8.25	219
ES0019U	41.39	2.12	80	NO0039R	62.78	8.88	210
ES0020U	37.16	-3.61	680	NO0042G	78.91	11.89	474
ES0021U	40.46	-3.73	669	NO0056R	60.37	11.08	300
ES0022R	42.05	0.73	1571	PL0005R	54.15	22.07	157
ES1778R	41.77	2.35	700	PL0009R	53.66	17.93	121
FI0009R	59.78	21.38	7	PL0010U	50.07	19.91	282
FI0036R	68.00	24.24	340	PT0004R	38.08	-8.80	43
FI0050R	61.85	24.28	181	PT0006R	38.74	-9.21	109
FR0008R	48.50	7.13	775	RO0010R	44.34	26.01	77
FR0009R	49.90	4.63	390	SE0011R	56.02	13.15	175
FR0013R	43.62	0.18	200	SE0022R	60.09	17.51	45
FR0018R	48.63	-0.45	309	SI0008R	45.57	14.87	520
FR0019R	42.94	0.14	2877				

This project has received funding from the European Union's Horizon Europe research and innovation programme under grant agreement No 101081395

Table 2. List of IMPROVE stations used.

Name	Latitude	Longitude	Altitude (m) asl	Name	Latitude	Longitude	Altitude (m) asl
ACAD1	44.38	-68.26	157	MAKA2	48.30	-124.62	480
AGTI1	33.46	-116.97	507	MAVI1	41.33	-70.78	2
ATLA1	33.69	-84.29	243	MEAD1	36.02	-114.07	902
BADL1	43.74	-101.94	736	MELA1	48.49	-104.48	606
BALA1	51.03	-115.03	1391	MEVE1	37.20	-108.49	2172
BALD1	34.06	-109.44	2508	MING1	36.97	-90.14	111
BAND1	35.78	-106.27	1988	MOHO1	45.29	-121.78	1531
BIBE1	29.30	-103.18	1066	MOMO1	41.82	-73.30	521
BIRM1	33.55	-86.81	175	MONT1	47.12	-113.15	1282
BLIS1	38.98	-120.10	2130	MOOS1	45.13	-67.27	77
BLIS2	38.98	-120.10	2130	MORA1	46.76	-122.12	439
BLMO1	43.72	-96.19	473	MOZI1	40.54	-106.68	3243
BOAP1	33.87	-106.85	1389	NEBR1	41.89	-100.34	883
BOLA1	42.85	-109.64	2296	NOAB1	44.74	-109.38	2482
BOND1	40.05	-88.37	263	NOCA1	48.73	-121.06	568
BOWA1	47.95	-91.50	526	NOCH1	45.65	-106.56	1283
BRCA1	37.62	-112.17	2481	NOGA1	31.34	-110.94	1172
BRID1	42.97	-109.76	2626	OKEF1	30.74	-82.13	48
BRIG1	39.47	-74.45	5	OLYM1	48.01	-122.97	599
BRIS1	30.11	-89.76	-7	ORPI1	31.95	-112.80	504
BRMA1	44.11	-70.73	233	OWVL1	37.36	-118.33	1234
BYIS1	37.97	124.63	100	PACK1	42.86	-71.88	695
CABA1	43.83	-70.06	26	PASA1	48.39	-119.93	1627
CABI1	47.95	-115.67	1441	PEFO1	35.08	-109.77	1766
CACO1	41.98	-70.02	49	PENO1	44.95	-68.65	45
CACR1	34.45	-94.14	683	PHOE1	33.50	-112.10	342
CANY1	38.46	-109.82	1798	PHOE5	33.50	-112.10	342
CAPI1	38.30	-111.29	1896	PINN1	36.48	-121.16	302
CAVE1	32.18	-104.44	1355	PITT1	40.47	-79.96	268
CEBL1	38.77	-99.76	665	PMRF1	44.53	-72.87	401
CHAS1	28.75	-82.55	4	PORE1	38.12	-122.91	97
CHIR1	32.01	-109.39	1554	PRIS1	46.70	-68.03	165
CLPE1	44.33	-106.96	2470	PUSO1	47.57	-122.31	97
COHU1	34.79	-84.63	735	QUCI1	39.94	-81.34	366
CORI1	45.66	-121.00	178	QURE1	42.30	-72.33	317

This project has received funding from the European Union's Horizon Europe research and innovation programme under grant agreement No 101081395

CRES1	41.76	-102.43	1207	QUVA1	33.29	-111.29	661
CRLA1	42.90	-122.14	1996	RAFA1	34.73	-120.01	956
CRMO1	43.46	-113.56	1817	REDW1	41.56	-124.08	243
DENA1	63.72	-148.97	658	ROMA1	32.94	-79.66	4
DETR1	42.23	-83.21	179	ROMO1	40.28	-105.55	2760
DINO1	40.25	-108.97	1829	SACR1	33.46	-104.40	1072
DOME1	35.73	-118.14	927	SAGA1	34.30	-118.03	1791
DOSO1	39.11	-79.43	1182	SAGO1	34.19	-116.91	1726
DOUG1	31.35	-109.54	1230	SAGU1	32.17	-110.74	941
EGBE1	44.23	-79.78	251	SAMA1	30.09	-84.16	7
ELDO1	37.70	-94.03	297	SAPE1	36.01	-106.84	2935
ELLI1	36.09	-99.94	697	SAWE1	32.25	-111.22	714
EVER1	25.39	-80.68	1	SAWT1	44.17	-114.93	1990
FCPC1	45.56	-88.81	564	SENE1	46.29	-85.95	214
FLAT1	47.77	-114.27	1580	SEQU1	36.49	-118.83	519
FLTO1	39.92	-107.63	2593	SHEN1	38.52	-78.43	1079
FOCO1	40.59	-105.14	1572	SHMI1	37.30	-107.48	2351
FOCO2	-999.00	-999.00	-999	SHRO1	35.39	-82.77	1617
FOPE1	48.31	-105.10	638	SIAN1	34.09	-110.94	1600
FRES1	36.78	-119.77	100	SIME1	55.33	-160.51	57
FRRE1	39.71	-79.01	767	SIPS1	34.34	-87.34	286
GAAR1	66.90	-151.52	196	SNPA1	47.42	-121.43	1049
GAMO1	46.83	-111.71	2387	SOGP1	36.61	-97.49	314
GICL1	33.22	-108.24	1775	STAR1	45.22	-118.51	1259
GLAC1	48.51	-114.00	975	STIL1	35.75	-94.67	300
GRBA1	39.01	-114.22	2065	SULA1	45.86	-114.00	1895
GRCA2	35.97	-111.98	2267	SWAN1	35.45	-76.21	-3
GRGU1	44.31	-71.22	453	SYCA1	35.14	-111.97	2046
GRRI1	43.94	-91.41	370	SYCA2	35.16	-111.98	2046
GRSA1	37.72	-105.52	2498	TALL1	38.43	-96.56	390
GRSM1	35.63	-83.94	810	THBA1	44.66	-105.29	1195
GUMO1	31.83	-104.81	1672	THRO1	46.89	-103.38	852
HACR1	20.76	-156.25	2158	THSI1	44.29	-122.04	885
HAVO1	19.43	-155.26	1258	TONT1	33.65	-111.11	775
HECA1	44.97	-116.84	655	TOOL1	68.63	-149.61	740
HEGL1	36.61	-92.92	404	TRCR1	62.32	-150.32	155
HOOV1	38.09	-119.18	2560	TRIN1	40.79	-122.80	1014
IKBA1	34.34	-111.68	1297	ULBE1	47.58	-108.72	891

This project has received funding from the European Union's Horizon Europe research and innovation programme under grant agreement No 101081395

ISLE1	47.46	-88.15	182	UPBU1	35.83	-93.20	722
JARB1	41.89	-115.43	1869	VIIS1	18.34	-64.80	51
JARI1	37.63	-79.51	289	VILA1	40.97	-95.05	371
JOSH1	34.07	-116.39	1235	VOYA2	48.41	-92.83	429
KAIS1	37.22	-119.15	2597	WASH1	38.88	-77.03	15
KALM1	42.55	-124.06	80	WEMI1	37.66	-107.80	2750
KPBO1	60.01	-151.71	5	WHIT1	33.47	-105.53	2063
LABE1	41.71	-121.51	1459	WHPA1	46.62	-121.39	1827
LASU2	40.69	-92.01	229	WHPE1	36.59	-105.45	3366
LAVO1	40.54	-121.58	1732	WHRI1	39.15	-106.82	3413
LIGO1	35.97	-81.93	968	WICA1	43.56	-103.48	1296
LOND1	42.86	-71.38	124	WIMO1	34.73	-98.71	509
LOST1	48.64	-102.40	696	YELL2	44.57	-110.40	2425
LTCC1	38.92	-119.98	1935	YOSE1	37.71	-119.71	1603
LYEB1	42.96	-72.91	882	ZICA1	37.20	-113.15	1215
MACA1	37.13	-86.15	235				

This project has received funding from the European Union's Horizon Europe research and innovation programme under grant agreement No 101081395

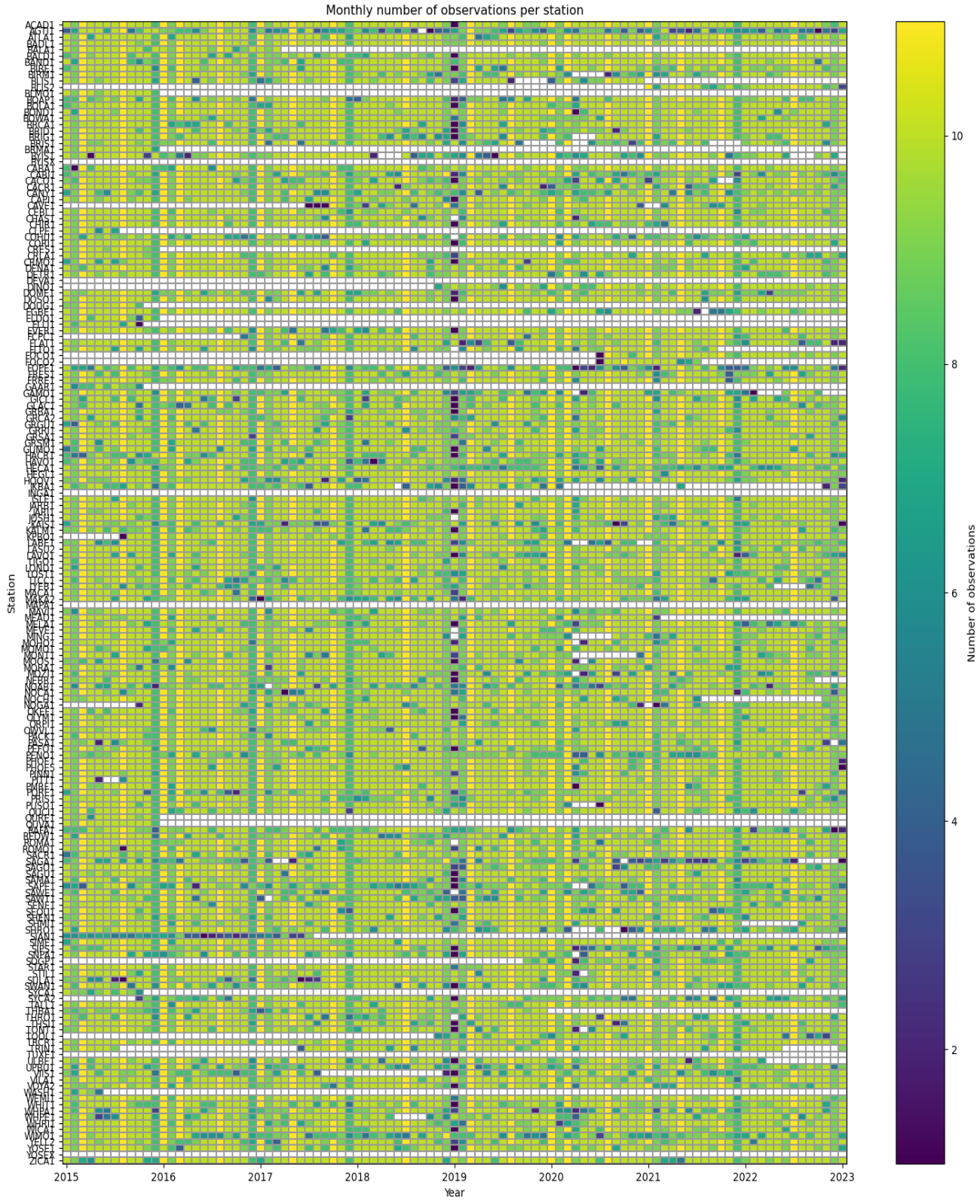

Fig. 6. IMPROVE stations with available EC observations for the period 2015 to 2023, the colored scale shows the number of available daily observations in each month

This project has received funding from the European Union's Horizon Europe research and innovation programme under grant agreement No 101081395

Table 3. List of Spartan, Putaud et al. and other acquired stations.

Name	Latitude	Longitude	Altitude (m) asl	Name	Latitude	Longitude	Altitude (m) asl
Spartan	-34.56	-58.51	26	Putaud et al.	-16.51	-68.20	4025
Spartan	23.73	90.4	34	Putaud et al.	-16.50	-68.13	3600
Spartan	43.79	-79.47	186	Putaud et al.	32.05	118.62	20
Spartan	45.38	-71.93	251	Putaud et al.	38.03	114.53	83
Spartan	40	116.33	92	Putaud et al.	7.01	100.50	13
Spartan	9.01	38.82	2370	Putaud et al.	40.00	118.70	39
Spartan	-6.89	107.61	826	Putaud et al.	39.38	117.04	5
Spartan	32.78	35.02	230	Putaud et al.	39.76	116.95	36
Spartan	31.91	34.81	73	Putaud et al.	40.40	117.58	579
Spartan	22.65	120.31	3	Putaud et al.	36.95	116.60	370
Spartan	25.04	121.5	13	ALTZ	19.12	-98.66	3985
Spartan	34.2	-118.17	366	AMTT	2.14	-59.00	2306
Spartan	21.05	105.8	40	CACTI	-32.16	-64.69	1141
Spartan	-26.18	28	1720	FKL	35.34	25.67	250
Spartan	-25.76	28.28	1449	FUKU	34.00	130.90	75
Putaud et al.	13.82	100.51	2	NSA	71.32	-156.61	11
Putaud et al.	38.87	115.45	25	RWND	-1.59	29.57	2590
Putaud et al.	39.97	116.37	44	SMCN	28.47	98.79	2306
Putaud et al.	4.66	-74.1	2600	VRNS	25.27	82.98	80
Putaud et al.	-16.35	-68.13	5240	WLGG	-26.57	26.94	1480
Putaud et al.	18.48	98.57	300				

This project has received funding from the European Union's Horizon Europe research and innovation programme under grant agreement No 101081395

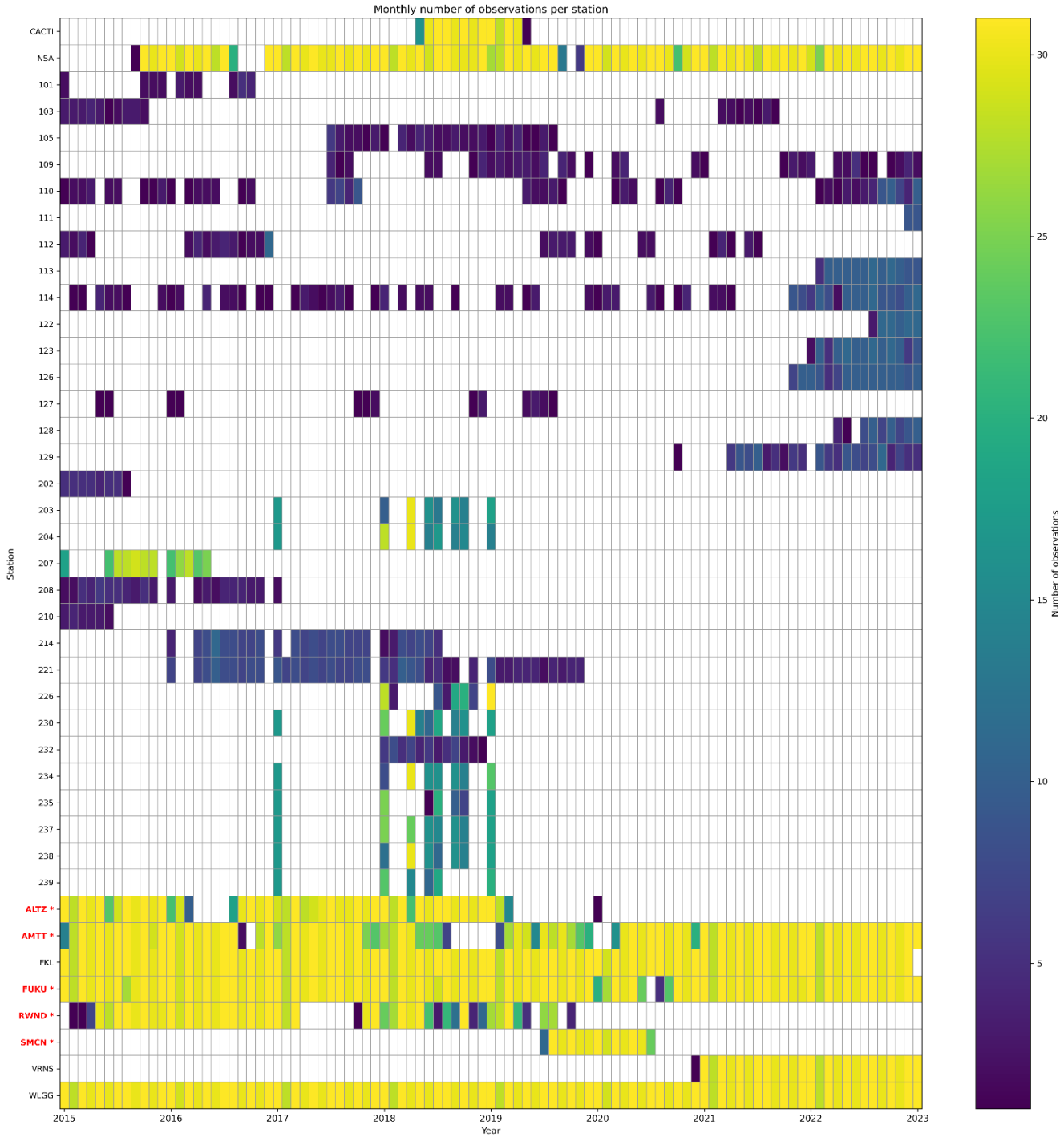

Fig 7. Other stations with EC and eBC not yet included in EBAS or IMPROVE. With red color are marked the stations that are not used in the inversions presented here.

While over South America, we could collect observations from 2015-2019, the Indian networks had data available only after 2020. This hinders an accurate description of the geographical distribution and temporal evolution of the BC emissions.

This project has received funding from the European Union's Horizon Europe research and innovation programme under grant agreement No 101081395

When considering other observations than the aerosol absorption coefficient then two other global networks are available and used in the inversions. One is the SPARTAN network (The Surface PARTiculate mAtter Network). SPARTAN is a global, long-term initiative focused on analyzing the chemical and physical characteristics of aerosols collected through filter-based sampling at locations around the world (https://www.spartan-network.org/; Snider et al., 2016). It provides open-access data on particulate matter concentrations and composition, specifically targeting PM2.5 and PM10. The network aims to support the validation and refinement of remote sensing models and to aid efforts in air quality management. Currently, SPARTAN operates 29 monitoring sites across the globe. Aerosol samples are typically collected over 8-day intervals, from which the chemical constituents are subsequently analyzed.

In addition, we initiated collaboration with scientists in India and China, to also access data from these regions to improve the observation coverage there and to achieve a better uncertainty reduction. Figure 4 shows the location of the stations used for the here reported inversions with TM5MP-CTDAS for the period 2015-2023. FLEXINVERT used the same observations except over Europe (which is the focus of the joint PARIS-EYE-CLIMA deliverables, D3.8 and D3.12) and the IMPROVE network. This shows that North America and Europe are well constrained, South East Asia has some constraints, while little data are available from the other regions for the studied period.

2.6 Global BC Emissions from anthropogenic sources and from wildfires

In this project, FLEXINVERT is using global anthropogenic BC emissions at 0.5° resolution created for EYECLIMA and the HTAP experiments. Emissions are available for the years only for the years 2015 and 2020 for 8 different source categories (agricultural waste burning, domestic heating, shipping, industry and energy production). Anthropogenic emissions also include seasonal cycles in the domestic burning sector. In order to have more realistic annual emissions a linear interpolation for each gridcell and each month was performed to avoid stepwise increase.

The wildfire emissions are taken from GFAS/CAMS at daily resolution extracted from a 0.1° raster and aggregated to 0.5° to match the anthropogenic emissions. The average annual total is 6 Tg/year. However, at high latitudes the wildfire emissions dominate the anthropogenic emissions. The most severe fires are found in boreal regions in Canada and Siberia. The extreme maximum in Canadian fires in 2023 had a direct impact on air quality in Canada and the United States. Due to the high latitudes the fires also have an impact on the Arctic.

This project has received funding from the European Union's Horizon Europe research and innovation programme under grant agreement No 101081395

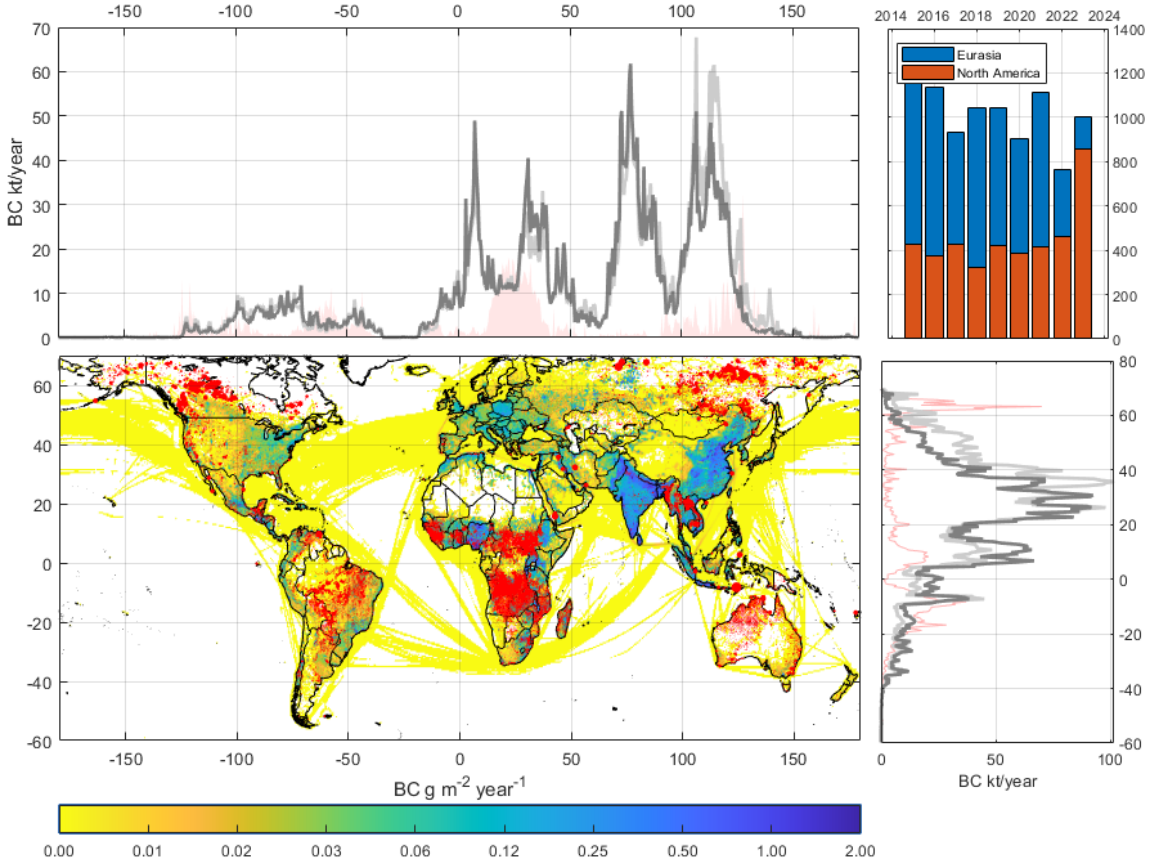

Figure 8: Source strength and spatial distribution of anthropogenic BC emissions. Panels top-left and bottom-right show the accumulated emission flux for each 0.5° longitude and latitude band, respectively, for the areas shown in panels bottom-left (grey) and topright (red). The geographical variability between Eurasia and North America of BC emission from wildfires for the study period of 2015-2023 is shown in panel top-right.

Regionally, the highest anthropogenic BC emissions are found in Asia, particularly South and East Asia. India and China are among the largest emitters due to their high population densities, extensive use of solid fuels, and growing transportation and industrial sectors. Sub-Saharan Africa also contributes significantly, primarily from residential biofuel use and open biomass burning, such as savanna and agricultural fires. Southeast Asia and parts of Latin America (notably the Amazon basin) experience large episodic emissions from agricultural and forest fires. In contrast, Europe and North America have lower emissions, primarily due to stricter emission standards and cleaner technologies, although urban areas with heavy diesel traffic can still be hotspots (Fig. 8).

The annual cycle of BC emissions and concentrations is strongly influenced by seasonal human activities and meteorological conditions. In regions with strong winter heating demand, such as northern India, China, and Eastern Europe, BC levels peak during the colder months due to increased residential combustion. Similarly, biomass burning seasons in tropical and subtropical regions, such as the dry season in central Africa or the pre-monsoon season in South Asia, are associated with pronounced increases in black carbon emissions. Wildfire-prone regions in North America, Siberia, and Australia exhibit seasonal spikes during the respective summer or dry seasons, when high temperatures and drought conditions promote fire activity.

This project has received funding from the European Union's Horizon Europe research and innovation programme under grant agreement No 101081395

TM5MP-CTDAS inversions reported here are using CMIP6 anthropogenic emissions and GFED biomass burning emissions. Anthropogenic emissions maximize in North Hemisphere winter while biomass burning in July-August-September as shown in Fig. 9 for the year 2020. According to these inventories, global anthropogenic emissions maximize in winter and biomass burning emissions in summer/fall Northern Hemisphere.

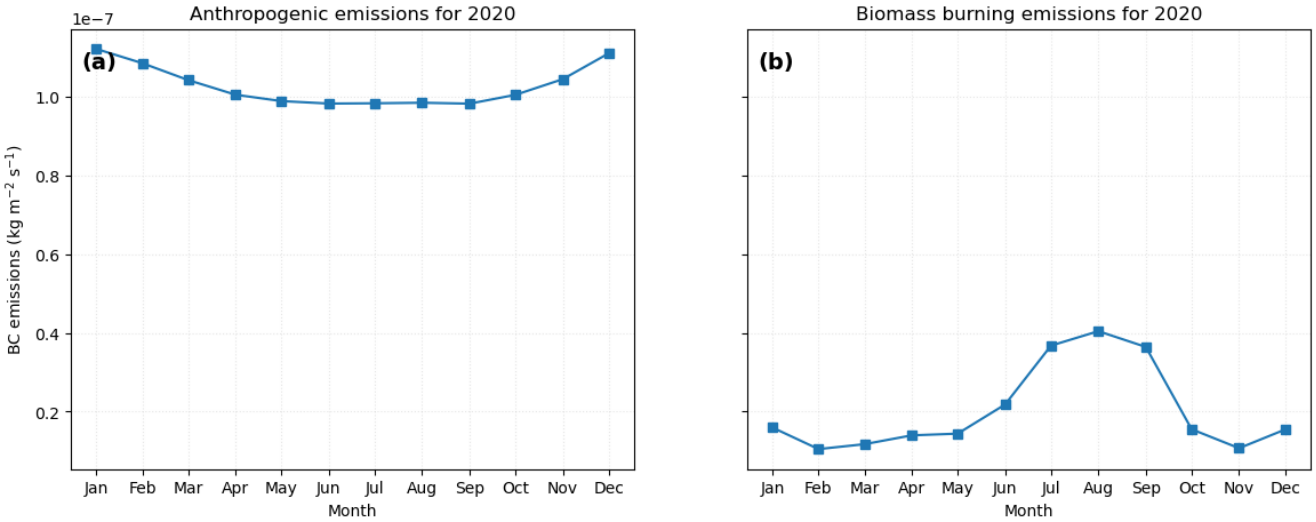

Figure 9. Global BC anthropogenic (CMIP6) (a) and biomass burning (GFED) (b) priori emissions used in TM5MP-CTDAS for the year 2020.

2.7 Deviations from the Description of Work

The global inversions are numerically complex and CPU demanding and this led to a delay in performing them and delivering the results compared to the initially planned timeline.

This project has received funding from the European Union's Horizon Europe research and innovation programme under grant agreement No 101081395

3. Results

The following estimates are the results of two different modelling and inversion approaches. The first approach uses a Lagrangian model (FLEXPART) in a Bayesian variational inversion framework, and the second approach uses a Eulerian model (TM5MP) with an Ensemble Kalman Filter (EnKF). The inversions also start from different prior emissions and describe differently the BC atmospheric transport, mixing and aging in the atmosphere. Together, their posterior emissions should span a large part of the uncertainty space associated with the uncertainties in atmospheric transport, scavenging and the dependence on the prior emissions estimate.

3.1 FLEXINVERT model results

We performed a global inversion for the years 2015 to 2022 with the stations that were available for each year. Fig. 10 shows the correction to the prior emissions through the inversion and Fig. 11 shows the prior and posterior emission comparisons per region. As can be seen in Fig. 2, the world highest emissions are in India, also China has significant BC emissions. Due to a lack of available observations in India and China, the emissions there are constrained by observations at stations in Japan and Korea, which receive air masses from these regions and hence are sensitive to the emissions there.

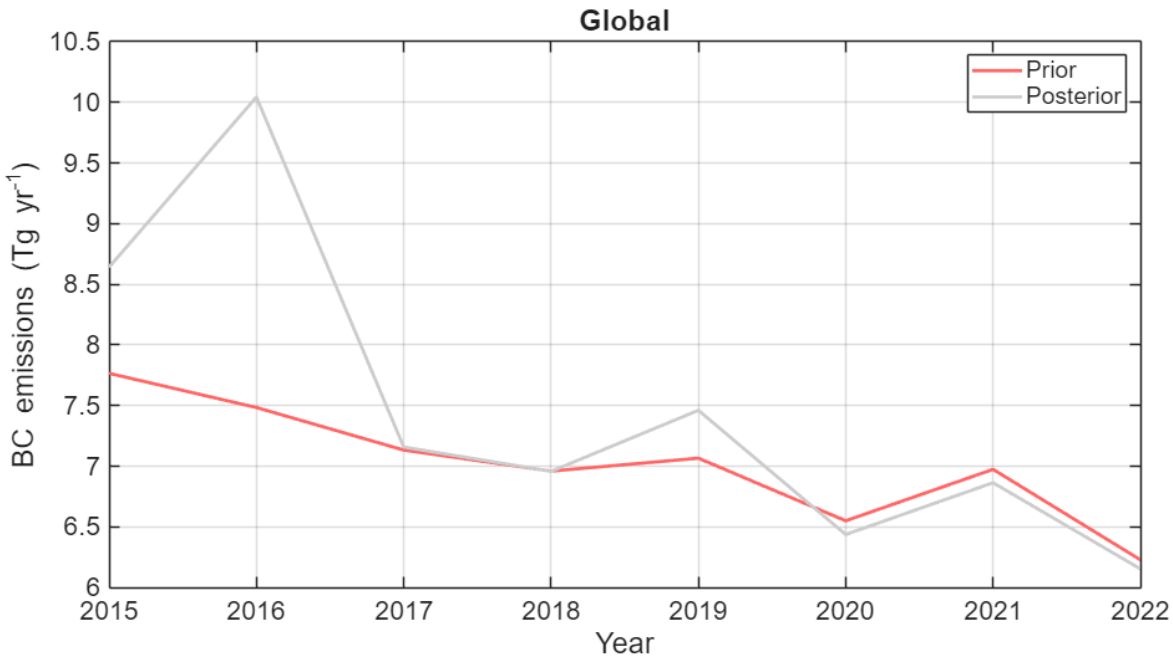

Fig. 10. Prior and posterior BC global emission estimates using FLEXINVERT for the years 2015 to 2023

This project has received funding from the European Union's Horizon Europe research and innovation programme under grant agreement No 101081395

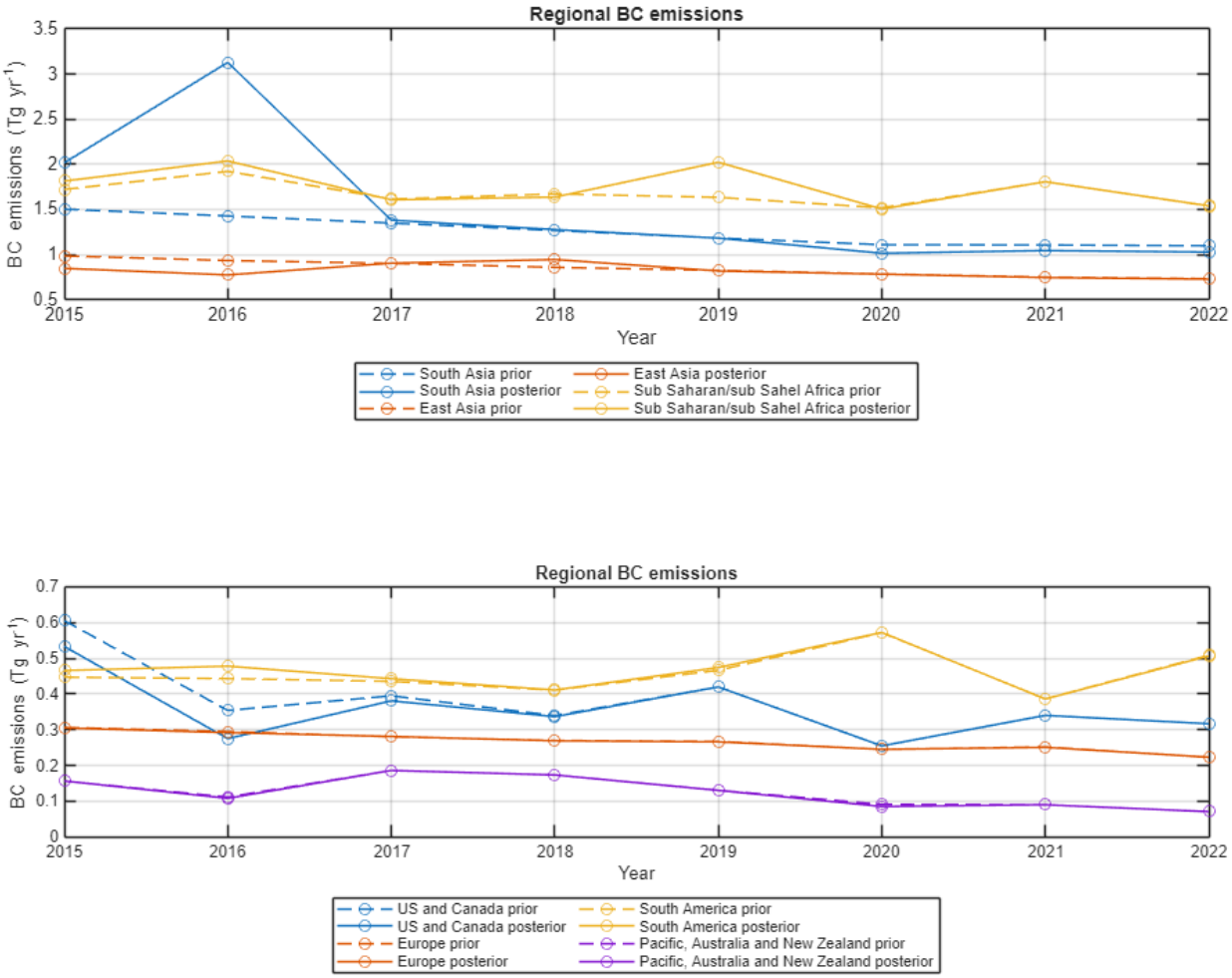

Fig. 11. Regional comparison of prior and posterior emissions calculated with FLEXINVERT for the years 2015 to 2023. Note that the scales in the two panels are different.

Most emission corrections are found over Asia, which is also the region with the highest BC emissions globally. Therefore, Fig. 12 focuses on India and China, where the largest inversion-induced adjustments occur. In the inversion using only the long-term monitoring stations, a negative correction is obtained in western India around the Delhi region, while emissions are increased in eastern India near Varanasi. When additional observational constraints from the Putaud et al (2025) and SPARTAN campaigns are included, the inversion produces a more coherent regional pattern, with emissions being systematically increased across large parts of India and reduced over China. This indicates that the additional observations provide important constraints in regions that are otherwise poorly represented by the routine monitoring network, leading to a redistribution of emissions within Asia and highlighting the sensitivity of the inversion results to observational coverage.

This project has received funding from the European Union's Horizon Europe research and innovation programme under grant agreement No 101081395

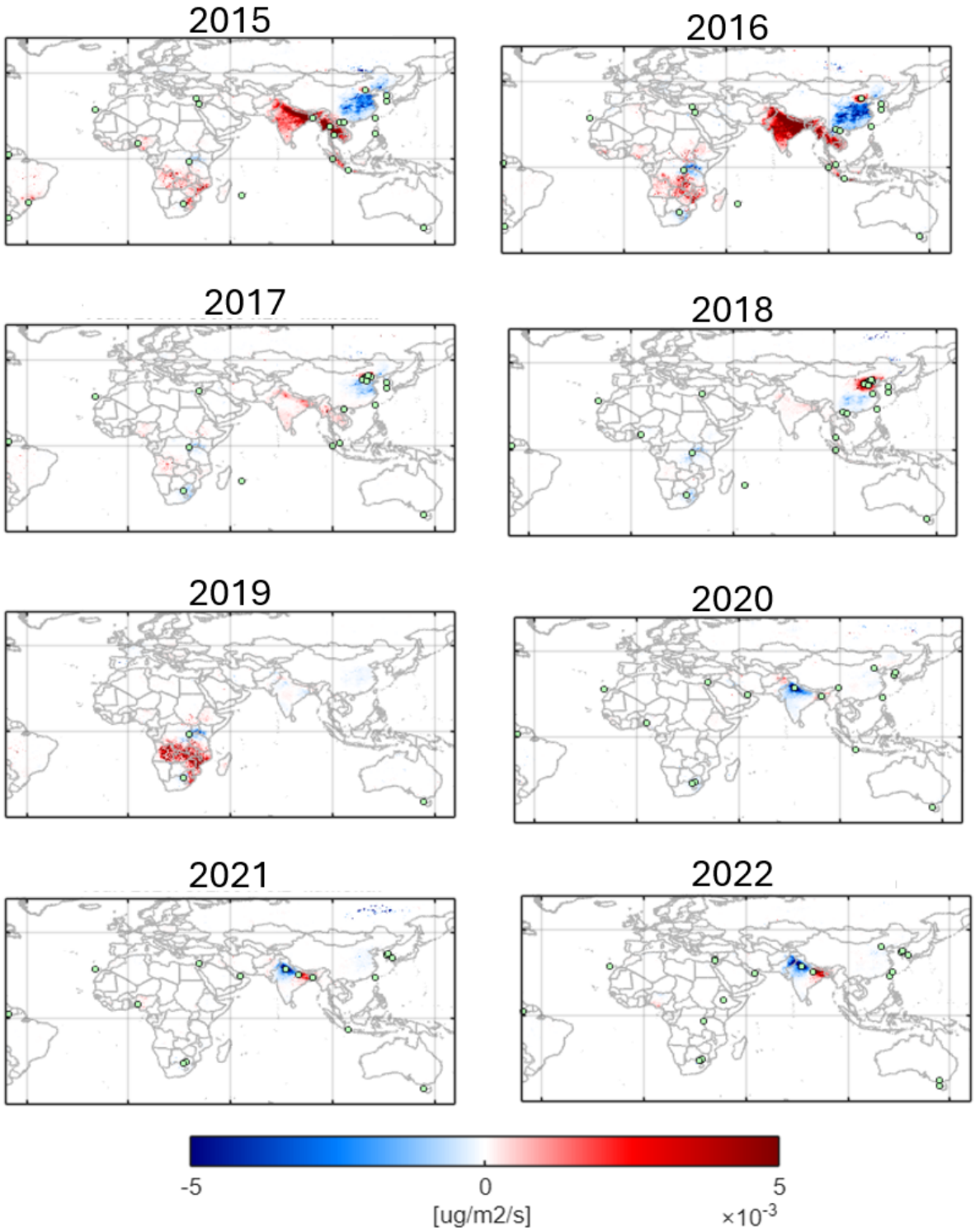

Figure 12: Global inversion results using FLEXINVERT for the years 2015 - 2022. The blue regions suggest a downward correction of the EYECLIMA prior emissions estimate and the red areas suggest an increase. The green dots indicate the location of the observations which have been used for the inversion in each year.

This project has received funding from the European Union's Horizon Europe research and innovation programme under grant agreement No 101081395

3.2 TM5MP-CTDAS model results

The annual global mean emissions of BC used in TM5MP-CTDAS (Prior) are shown in Fig.13 together with calculated posterior emissions for the years 2015-2023. For all studied years the prior emissions significantly exceed the posterior estimates with the largest differences calculated for the recent years. The uncertainty of the posterior estimate in this figure is calculated as the standard deviation of posterior emissions over the 50-member ensemble.

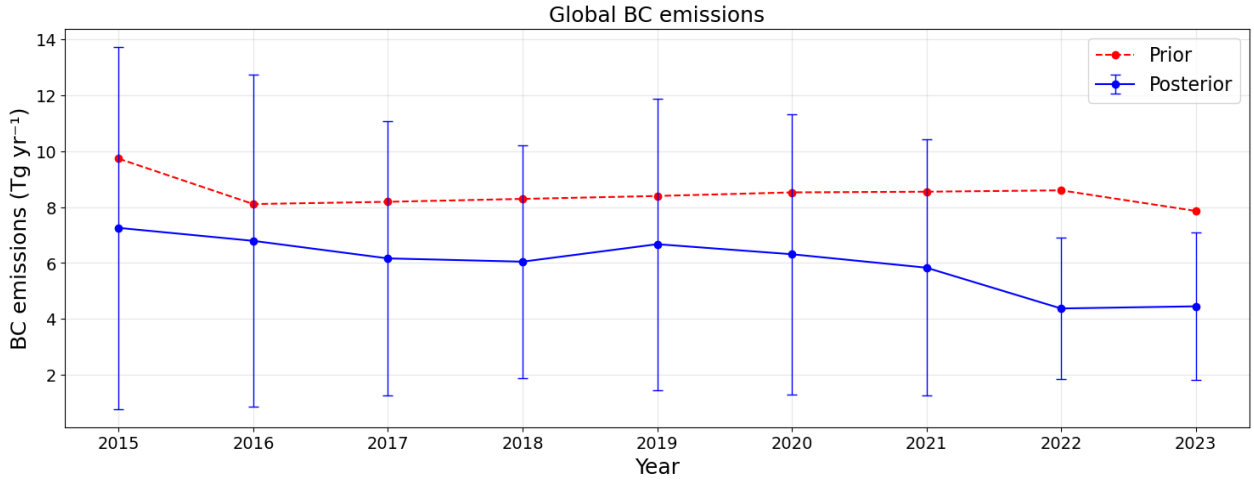

Fig. 13. Prior and posterior BC global emission estimates using TM5MP-CTDAS model for the years 2015 to 2023. The uncertainty in the posterior emissions was calculated from the ensemble. For each region, the standard deviation of the ensemble-member scaling factors was calculated and then multiplied by the corresponding regional emission mass. The regional uncertainties were then summed to estimate the deviation shown in the error bars, assuming no correlation between regions.

This project has received funding from the European Union's Horizon Europe research and innovation programme under grant agreement No 101081395

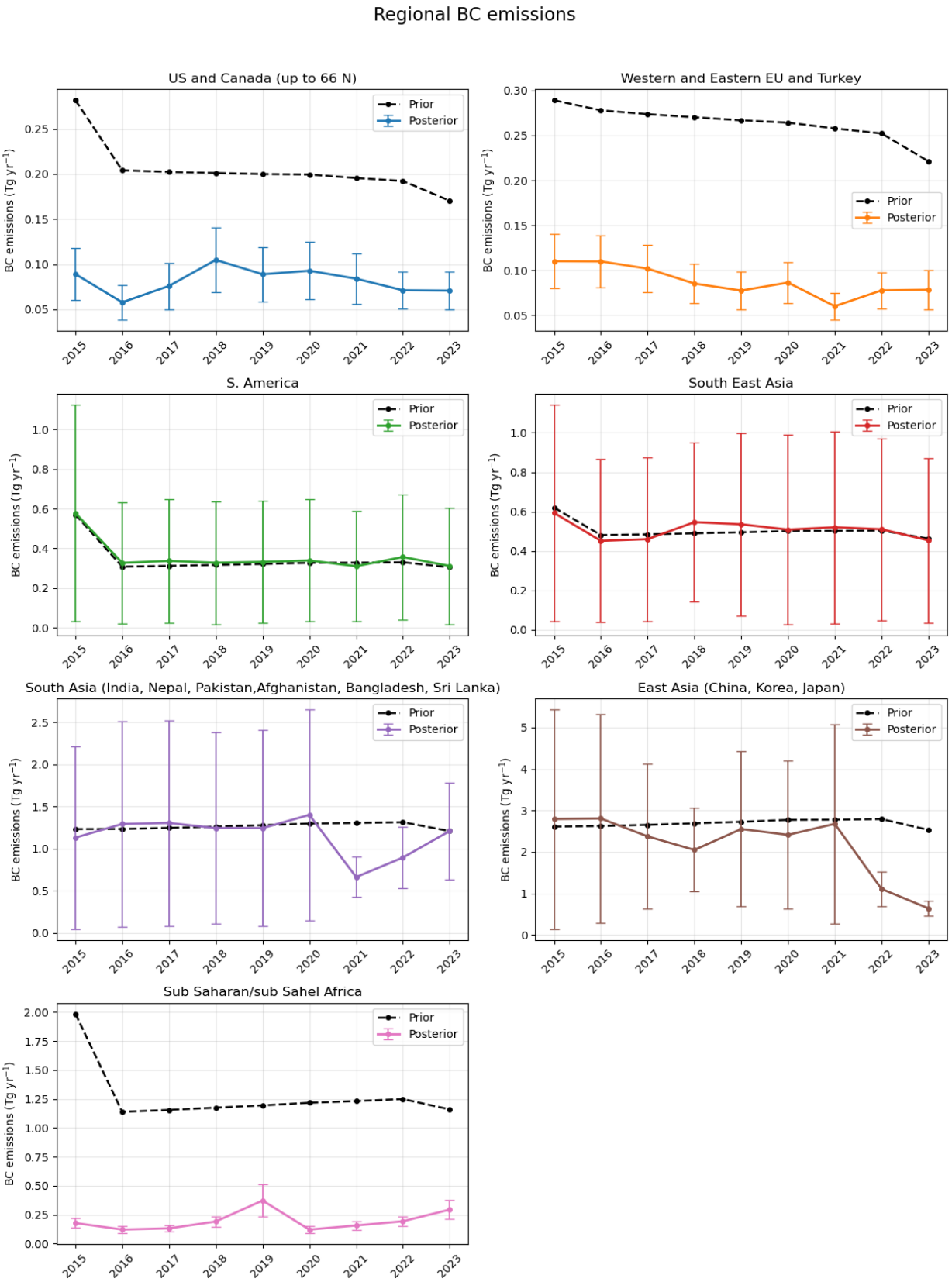

Fig.14: Regional comparison of prior and posterior emissions calculated with TM5MP-CTDAS

This project has received funding from the European Union's Horizon Europe research and innovation programme under grant agreement No 101081395

We further present the optimized global distribution of BC emissions averaged over the study period (Fig. 15) as well as the difference between the posterior and the prior emissions and the percent change due to optimization (Fig. 16). Figure 15 shows that BC emissions are highest over China and India and sub-Sahara/sub Sahel Africa. The posterior emissions show significant absolute emission reduction over these regions (Fig. 16a), while the highest percent changes are calculated over Africa, followed by Europe and North America. It is worth mentioning here that Africa emissions are constrained only by three stations as shown in Fig.4 and none of those stations is in the intensive biomass burning region. Therefore, the inversions are expected to miss information of this intensive source of BC and emission estimates as well as uncertainty reduction (Fig. 17) in this region have to be viewed with caution.

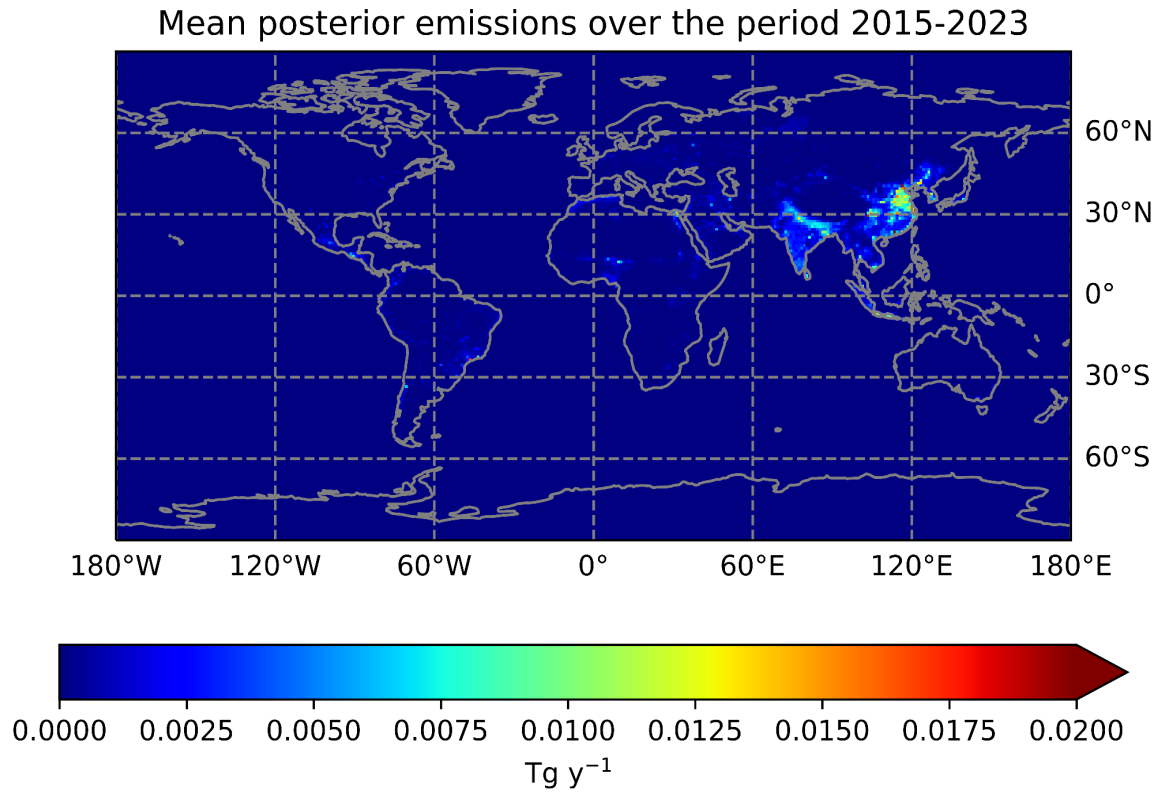

Fig. 15 Optimized global distribution of BC emissions averaged over 2015-2023 in 1ºx1º grid.

This project has received funding from the European Union's Horizon Europe research and innovation programme under grant agreement No 101081395

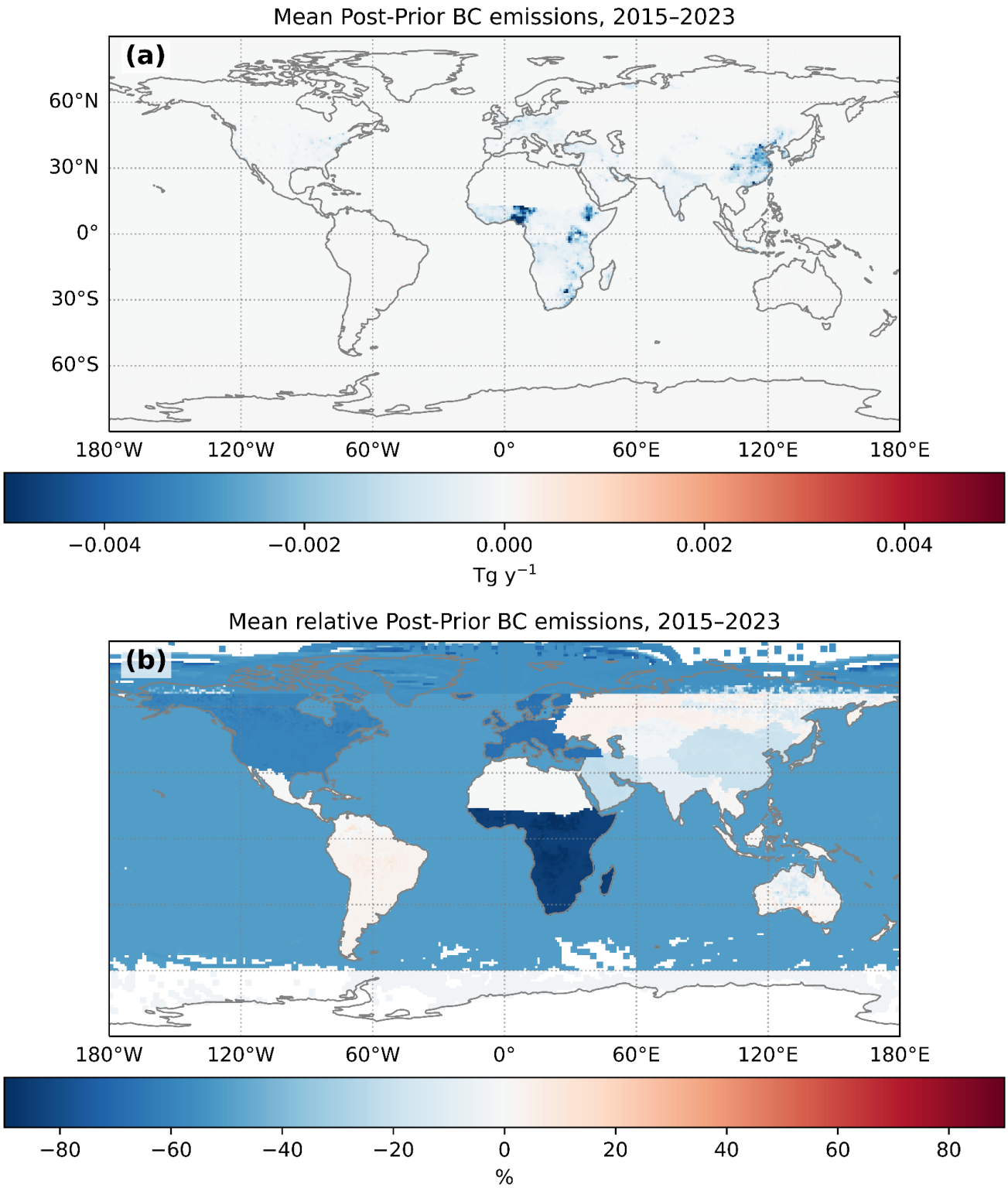

Fig. 16 (a) Change in posterior BC emissions relative to the prior emissions averaged over 2015-2023. Results are shown in 1°x1° grid; (b) percent change due to optimization [100 (Posterior_Prior)/Prior] for the considered HTAP regions.

This project has received funding from the European Union's Horizon Europe research and innovation programme under grant agreement No 101081395

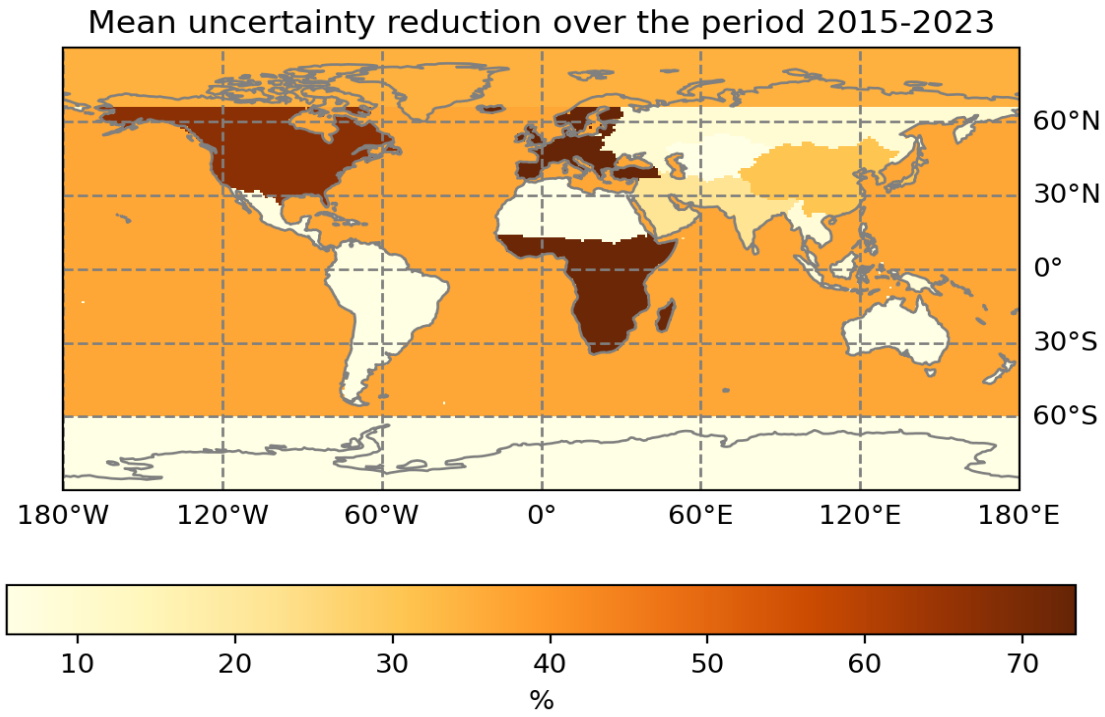

Fig. 17 Uncertainty reduction over the period of the inversion (2015-2023) per HTAP region.

Uncertainty reduction (UR) is calculated as the fraction of uncertainty after the inversion:

$$UR = 1 - \frac{\sigma_{posterior}}{\sigma_{prior}} 100\% \quad (1)$$

Where σ posterior and prior are the ensemble member standard deviation of the correction factors λ before and after the assimilation respectively. The large uncertainty reduction over Africa given that there are only a few stations there, will be further investigated.

3.3 Comparison of FLEXINVERT and TM5MP-CTDAS posterior emissions

Table 4 compares the inversion performed with the two independent modeling frameworks. FLEXINVERT based on a lagrangian model and EYCLIMA/HTAP prior emissions and TM5MP-CTDAS based on an eulerian model and CMIP6 emissions. Both modelling frameworks calculated lower global posterior than prior emissions after 2020, while from 2015 to 2019 the global posterior emissions calculated by FLEXINVERT are higher than the prior emissions. TM5MP-CTDAS calculates consistently lower posterior than prior BC emission across all studied years.

Largest absolute differences in the posterior emission estimates between the two different inversion frameworks are found for South Africa (SAF), South Asia (SAS), and East Asia (EAS) regions. These are areas with relatively little observational constraints. Accuracy improvement and better convergence of the posterior emissions would benefit from a more dense observational network in these regions. The differences in the Asian regions (SEA, SAS, EAS), maybe partly attributed to the fact that TM5-CTDAS didn't yet include all the available stations in the area during the inversion. Similarly TM5MP-CTDAS applies very large reductions in Sub-Saharan Africa often ~90%. In contrast FLEXINVERT keeps the posterior totals close to the prior. This suggests that the two models behave in a different way in the cases where observations

This project has received funding from the European Union's Horizon Europe research and innovation programme under grant agreement No 101081395

are sparse. The range of the posterior emission estimates calculated by the TM5MP-CTDAS 50 ensemble members is rather large and comprises the posterior emission estimates by FLEXINVERT.

However, when comparing FLEXINVERT and TM5MP-CTDAS posterior emission a global decreasing trend over the years is found. For the FLEXINVERT framework the emission decrease from 7.5 to 6.0 Tg/y, and in TM5MP-CTDAS from circa 7.5 to 4.5 Tg/y from 2015 to 2022. The fact that TM5MP-CTDAS finds a similar decreasing trend to flexinvert despite no trend in its prior is encouraging.

Table 4. BC global emission prior and posterior estimates and associated uncertainties. Units are Tg y^{-1}. The shown uncertainty in the posteriori emission estimates by TM5-CTDAS is the standard deviation of the 50 ensemble members posteriori emission estimates.

Year	**FLEXINVERT**		**TM5MP-CTDAS**	
	Prior	**Posterior**	**Prior**	**Posterior**
2015	7.77	8.64	9.73	7.25 ± 6.48
2016	7.48	10.04	8.11	6.79 ± 5.93
2017	7.13	7.16	8.19	6.16 ± 4.91
2018	6.96	6.96	8.29	6.05 ± 4.16
2019	7.07	7.46	8.40	6.67 ± 5.21
2020	6.55	6.44	8.52	6.31 ± 5.01
2021	6.97	6.86	8.55	5.83 ± 4.58
2022	6.23	6.15	8.60	4.37 ± 2.52
2023	-	-	7.86	4.45 ± 2.64

This project has received funding from the European Union's Horizon Europe research and innovation programme under grant agreement No 101081395

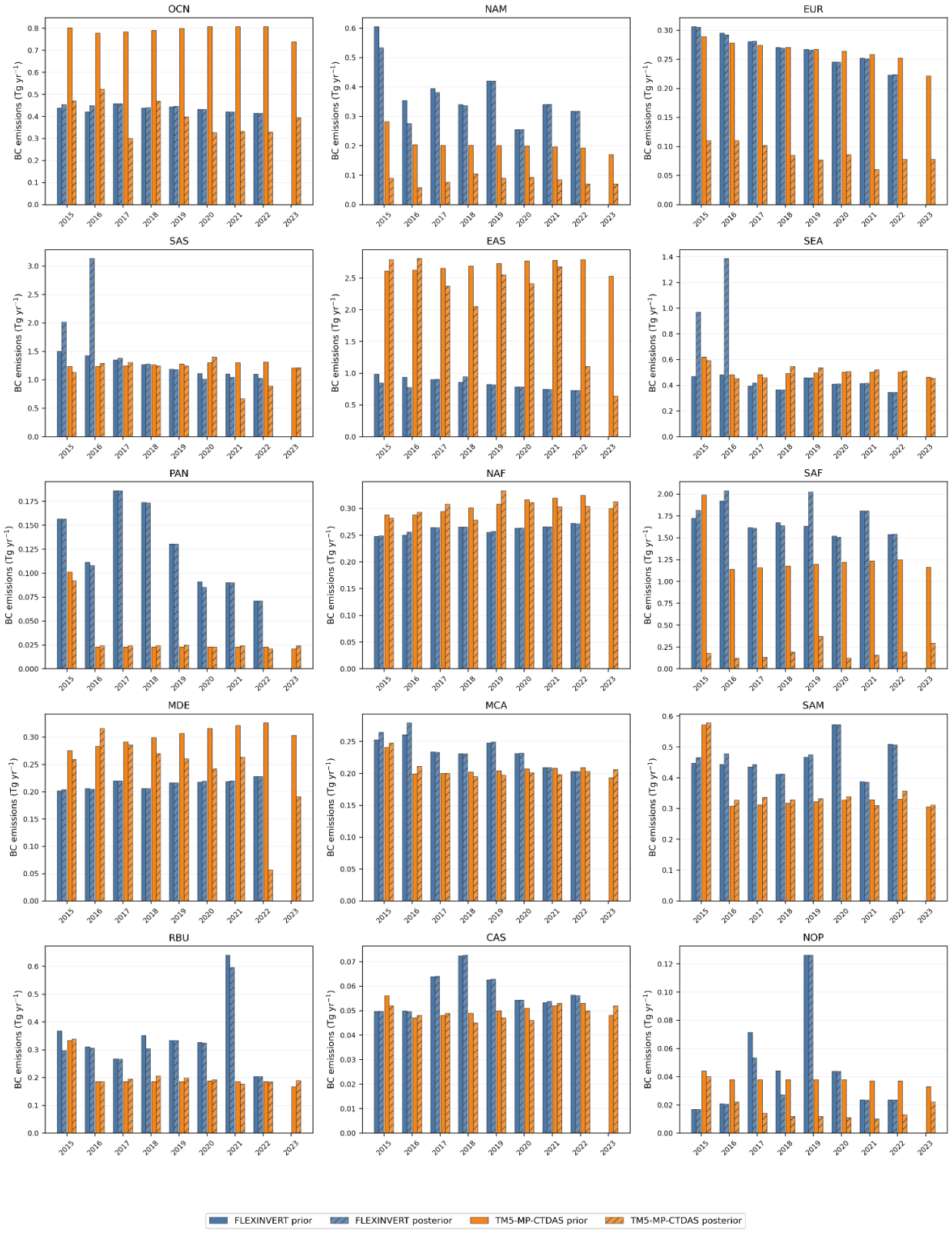

Figure 18. Annual BC regional emission prior and posterior estimates for the years 2015-2023. Units are Tg y^{-1}.

This project has received funding from the European Union's Horizon Europe research and innovation programme under grant agreement No 101081395

4. Conclusion and outlook

The two inversion systems result in somewhat different global BC emissions. However, at least for the years 2018 to 2021 the global emission estimates from the two inversions converge, being closer than the prior estimates used in each inversion.

In the TM5MP-CTDAS framework, the optimized posterior emissions are consistently lower than the prior estimates throughout the study period (2015-2023). Prior emissions remain relatively stable, ranging from approximately 7.9 to 9.7 Tg yr^{-1}, whereas the posterior estimates are substantially lower in the early years and decrease even more after optimization, particularly between 2021 and 2023. The largest downward adjustments occurs during the most recent years, where posterior emissions are 2-4 Tg yr^{-1} lower than the prior estimates. This behaviour suggests that the prior inventory used within TM5MP-CTDAS, based on CMIP6 emissions, overestimates the emissions required to reproduce the observed BC concentrations and that the inversion systematically compensates by decreasing emissions. The posterior estimates a stronger gradual decline in global BC emissions over the study period compared to the prior.

In contrast, the FLEXINVERT inversion starts from considerably lower prior emissions compared to those used in TM5MP-CTDAS, with global BC emissions ranging from about 6.2 to 7.8 Tg yr^{-1}. The optimization increases emissions, particularly in 2015 and 2019 by approximately 0.8-1.0 Tg yr^{-1}. For later years, the posterior estimates remain below the prior values, indicating that the observations are better reproduced with lower emissions than assumed in the HTAP-based prior inventory. The upward correction in the first years stems mainly from South and South-East Asia.

Despite these contrasting responses, the posterior emission estimates from the two inversion systems become more similar than the corresponding prior estimates for the years 2018-2021. This small convergence suggests that the observational constraints for these years drive both inversion systems toward a more consistent range of global BC emissions.

The inversions need to be validated against independent observations as those of the AERONET network which provide absorption aerosol optical depth (AAOD) values. Note however that observed AAOD includes all absorbing aerosol components i.e. in addition to BC, brown carbon and dust have to be taken into consideration in the model AAOD for a fair comparison. Therefore, potential modeling errors in the representation of brown carbon and dust have to be taken into consideration when analyzing the results.

Our inversions show the importance of a geographically representative observational database with good temporal coverage based on a coordinated and intercalibrated network of background stations of BC. The compilation effort started by Putaud et al (2025) demonstrates the need for further BC observations, particularly over North Asia, Middle East and the Global South. Such observations will further constraint the BC emissions.

This project has received funding from the European Union's Horizon Europe research and innovation programme under grant agreement No 101081395

5. References

Bakels, L., Tatsii, D., Tipka, A., Thompson, R., Dütsch, M., Blaschek, M., Seibert, P., Baier, K., Bucci, S., Cassiani, M., Eckhardt, S., Groot Zwaaftink, C., Henne, S., Kaufmann, P., Lechner, V., Maurer, C., Mulder, M. D., Pisso, I., Plach, A., Subramanian, R., Vojta, M., and Stohl, A.: FLEXPART version 11: improved accuracy, efficiency, and flexibility, Geosci. Model Dev., 17, 7595–7627, https://doi.org/10.5194/gmd-17-7595-2024, 2024.

Snider, G., Weagle, C. L., Murdymootoo, K. K., Ring, A., Ritchie, Y., Stone, E., Walsh, A., Akoshile, C., Anh, N. X., Balasubramanian, R., Brook, J., Qonitan, F. D., Dong, J., Griffith, D., He, K., Holben, B. N., Kahn, R., Lagrosas, N., Lestari, P., Ma, Z., Misra, A., Norford, L. K., Quel, E. J., Salam, A., Schichtel, B., Segev, L., Tripathi, S., Wang, C., Yu, C., Zhang, Q., Zhang, Y., Brauer, M., Cohen, A., Gibson, M. D., Liu, Y., Martins, J. V., Rudich, Y., and Martin, R. V.: Variation in global chemical composition of $PM_{2.5}$: emerging results from SPARTAN, Atmos. Chem. Phys., 16, 9629–9653, https://doi.org/10.5194/acp-16-9629-2016, 2016.

Choi, M., Lyapustin, A., Schuster, G. L., Go, S., Wang, Y., Korkin, S., Kahn, R., Reid, J. S., Hyer, E. J., Eck, T. F., Chin, M., Diner, D. J., Kalashnikova, O., Dubovik, O., Kim, J., and Moosmüller, H.: Light-absorbing black carbon and brown carbon components of smoke aerosol from DSCOVR EPIC measurements over North America and central Africa, Atmos. Chem. Phys., 24, 10543–10565, https://doi.org/10.5194/acp-24-10543-2024, 2024.

Feng, L., Smith, S. J., Braun, C., Crippa, M., Gidden, M. J., Hoesly, R., Klimont, Z., van Marle, M., van den Berg, M., and van der Werf, G. R.: The generation of gridded emissions data for CMIP6, Geosci. Model Dev., 13, 461–482, https://doi.org/10.5194/gmd-13-461-2020, 2020.

Gogoi, M. M., Babu, S. S., Imasu, R., and Hashimoto, M.: Satellite (GOSAT-2 CAI-2) retrieval and surface (ARFINET) observations of aerosol black carbon over India, Atmos. Chem. Phys., 23, 8059–8079, https://doi.org/10.5194/acp-23-8059-2023, 2023.

Kumar, P.; Garg, A.; Sharma, K.; Nadeem, U.; Sarma, K.; Gupta, N.C.; Kumar, A.; Pandey, A.K. Seasonal and Spatial Variations in Particulate Matter, Black Carbon and Metals in Delhi, India's Megacity. *Urban Sci. 8*, 101. https://doi.org/10.3390/urbansci8030101, 2024.

Malm, W. C., J. F.Sisler, D.Huffman, R. A.Eldred, and T. A.Cahill : Spatial and seasonal trends in particle concentration and optical extinction in the United States, J. Geophys. Res., 99(D1), 1347–1370, doi:10.1029/93JD02916., 1994.

Pisso, I., Sollum, E., Grythe, H., Kristiansen, N. I., Cassiani, M., Eckhardt, S., Arnold, D., Morton, D., Thompson, R. L., Groot Zwaaftink, C. D., Evangeliou, N., Sodemann, H., Haimberger, L., Henne, S., Brunner, D., Burkhart, J. F., Fouilloux, A., Brioude, J., Philipp, A., Seibert, P., and Stohl, A.: The Lagrangian particle dispersion model FLEXPART version 10.4, Geosci. Model Dev., 12, 4955–4997, https://doi.org/10.5194/gmd-12-4955-2019, 2019.

Putaud, J.-P., Cavalli, F., Yttri, K.E., Chow, J.C.,et al.: A worldwide aerosol phenomenology: Elemental and organic carbon in PM2.5 and PM10, Atmospheric Environment, 358, 121338, https://doi.org/10.1016/j.atmosenv.2025.121338, 2025.

Ren, Y., Oxford, C.R., Zhang, D. *et al.* Black carbon emissions generally underestimated in the global south as revealed by globally distributed measurements. *Nat Commun* **16**, 7010, https://doi.org/10.1038/s41467-025-62468-5, 2025.

Stohl, A., Klimont, Z., Eckhardt, S., Kupiainen, K., Shevchenko, V. P., Kopeikin, V. M., and Novigatsky, A. N.: Black carbon in the Arctic: the underestimated role of gas flaring and residential combustion emissions, Atmos. Chem. Phys., 13, 8833–8855, https://doi.org/10.5194/acp-13-8833-2013, 2013

Thompson, R. L. and Stohl, A.: FLEXINVERT: an atmospheric Bayesian inversion framework for determining surface fluxes of trace species using an optimized grid, Geosci. Model Dev., 7, 2223–2242, https://doi.org/10.5194/gmd-7-2223-2014, 2014.

This project has received funding from the European Union's Horizon Europe research and innovation programme under grant agreement No 101081395

Vignati, E., J. Wilson, and P. Stier, M7: An efficient size-resolved aerosol microphysics module for large-scale aerosol transport models, J. Geophys. Res., 109, D22202, doi:10.1029/2003JD004485, 2004.

van der Laan-Luijkx, I. T., van der Velde, I. R., van der Veen, E., Tsuruta, A., Stanislawska, K., Babenhauserheide, A., Zhang, H. F., Liu, Y., He, W., Chen, H., Masarie, K. A., Krol, M. C., and Peters, W.: The CarbonTracker Data Assimilation Shell (CTDAS) v1.0: implementation and global carbon balance 2001–2015, Geosci. Model Dev., 10, 2785–2800, https://doi.org/10.5194/gmd-10-2785-2017, 2017.

Wang, Y., Ju, Q., Xing, Z., Zhao, J., Guo, S., Li, F., Du, K.: Observation of black carbon in Northern China in winter of 2018–2020 and its implications for black carbon mitigation, Science of The Total Environment 877, 162897, https://doi.org/10.1016/j.scitotenv.2023.162897, 2023.

Williams, J. E., Boersma, K. F., Le Sager, P., and Verstraeten, W. W.: The high-resolution version of TM5-MP for optimized satellite retrievals: description and validation, Geosci. Model Dev., 10, 721–750, https://doi.org/10.5194/gmd-10-721-2017, 2017.

Yang, Z., Zhang, Y., Xie, Y., Xu, H., Yan, C., Hu, T., Li, Z.: Inversion of the global carbonaceous aerosol components (CACs) based on ground-based remote sensing of AERONET, Environment International, 198, 109432, https://doi.org/10.1016/j.envint.2025.109432, 2025.

Zhao, W., Zhao, Y., Zheng, Y., Chen, D., Xin, J., Li, K., Che, H., Li, Z., Ma, M., and Hang, Y.: Long-term variability in black carbon emissions constrained by gap-filled absorption aerosol optical depth and associated premature mortality in China, Atmos. Chem. Phys., 24, 6593–6612, https://doi.org/10.5194/acp-24-6593-2024, 2024.

Zhu, C., Kanaya, Y., Takigawa, M., Ikeda, K., Tanimoto, H., Taketani, F., Miyakawa, T., Kobayashi, H., and Pisso, I.: FLEXPART v10.1 simulation of source contributions to Arctic black carbon, Atmos. Chem. Phys., 20, 1641–1656, https://doi.org/10.5194/acp-20-1641-2020, 2020.

This project has received funding from the European Union's Horizon Europe research and innovation programme under grant agreement No 101081395

https://eyeclima.eu

BRUSSELS, 30 06 2026

Funded by the European Union. Views and opinions expressed are however those of the author(s) only and do not necessarily reflect those of the European Union. Neither the European Union nor the granting authority can be held responsible for them.

This project has received funding from the European Union's Horizon Europe research and innovation programme under grant agreement No 101081395